www.sciencemag.org/cgi/content/full/science.1228380/DC1

Supplementary Materials for

Kepler-47: A Transiting Circumbinary Multiplanet System

Jerome A. Orosz,* William F. Welsh, Joshua A. Carter, Daniel C. Fabrycky, William D. Cochran, Michael Endl, Eric B. Ford, Nader Haghighipour, Phillip J. MacQueen, Tsevi Mazeh, Roberto Sanchis-Ojeda, Donald R. Short, Guillermo Torres, Eric Agol, Lars A. Buchhave, Laurance R. Doyle, Howard Isaacson, Jack J. Lissauer, Geoffrey W. Marcy, Avi Shporer, Gur Windmiller, Thomas Barclay, Alan P. Boss, Bruce D. Clarke, Jonathan Fortney, John C. Geary, Matthew J. Holman, Daniel Huber, Jon M. Jenkins, Karen Kinemuchi, Ethan Kruse, Darin Ragozzine, Dimitar Sasselov, Martin Still, Peter Tenenbaum, Kamal Uddin, Joshua N. Winn, David G. Koch, William J. Borucki

*To whom correspondence should be addressed. E-mail: orosz@sciences.sdsu.edu

Published 28 August 2012 on *Science* Express
DOI: 10.1126/science.1228380

This PDF file includes:

Materials and Methods
Supplementary Text
Figs. S1 to S25
Tables S1 to S9
References (*25*–*59*)

Supporting Online Material (SOM)

We provide additional details regarding the detection and characterization of Kepler-47 in this supplement. §1.1 gives alternate designations and other information for Kepler-47. §1.2 discusses the Kepler data preparation and detrending. §1.3 discusses how the rotational period of the primary star is derived. §1.4 discusses the ground-based spectroscopic observations. §1.5 describes how the effective temperature, gravity, and metallicity of the primary were measured. §1.6 gives an overview of how the times of mid-eclipse for the primary and secondary eclipses were measured. §1.7 discusses the effects of star-spots on the measurement of the eclipse times and other parameters. §1.8 presents measurements of the transit times and the detection of a transit event possibly due to a third planet. §1.9 gives a full discussion of the photometric-dynamical model. §1.10 presents a discussion of independent light curve modeling done with the ELC code. §1.11 discusses how upper limits on the masses of the planets were derived. §1.12 considers the long-term stability of the planetary orbits. §1.13 gives a comparison of the stellar properties with evolutionary models. §1.14 presents details of the habitable zone in Kepler-47.

1 Materials and Methods

1.1 Alternate designations, celestial coordinates, and apparent magnitudes

Kepler-47 appears in the Kepler Input Catalog (*25*, KIC) as KIC 10020423. Other designations include Kepler Object of Interest KOI-3154 and 2MASS J19411149+4655136. The J2000 celestial coordinates given in the KIC are $\alpha = 19^{\rm h}41^{\rm m}11\overset{\rm s}{.}501$, $\delta = +46^\circ55'13\overset{''}{.}69$, and the apparent magnitudes are $r = 15.126$ and $\mathrm{Kp} = 15.178$.

1.2 Kepler data preparation and detrending

In this study we make use of data from Kepler Quarters Q1 through Q12 (May, 2009 through late March, 2012). We used the "simple aperture photometry" (SAP) provided by the Kepler pipeline and available at the Mikulski Archive for Space Telescopes (MAST). The Kepler SAP light curves show instrumental trends (*26*), so further processing is necessary. The detrending must be done for each Quarter separately since the object appears on a different detector module. The amount of detrending needed depends on the specific task. When modeling the eclipses and transits, a fairly aggressive detrending is used where both the instrumental trends and the spot modulations are removed. In this case, the eclipses and transits are masked out, and a high order cubic spline is fit to short segments whose end points are usually defined by gaps in the data collection due to monthly data downloads, rolls between Quarters, or spacecraft safe modes. The segments are normalized to the spline fits, and the segments are reassembled. The SAP light curves and the detrended light curve with the spot modulation removed are shown in Fig.

S1. Other tasks such as spot modeling require much less aggressive detrending, in which case low-order polynomials are used to stitch together different segments across the Quarters.

The time difference between the last Q12 observation and the first Q1 observation is 1050.51 days. During that interval, Kepler was collecting data 92.55% of the time, and 44389 cadences out of the 47580 in total were flagged as good (SAP_QUALITY=0), for a duty cycle of 86.34%. Not all observations with SAP_QUALITY$>$0 are necessarily useless, depending on the purpose, so the 86.34% duty cycle is a lower limit.

1.3 Rotational period from star-spot induced stellar variations

Fig. S2 shows closer-in views of the light curves from Q1, Q5, and Q9. A modulation of up to 3% in the out-of-eclipse regions due to star spots rotating into and out of view is evident. This modulation has a period that is close to, but not exactly equal to the eclipse (e.g. orbital) period. Fig. S3 depicts the autocorrelation of the cleaned detrended light curve, after the primary and secondary eclipses were removed and replaced by the value of the mean light curve with a typical random noise. The autocorrelation reveals clear modulation with a period of about 7.8 days. Presumably, the clock behind the modulation is the stellar rotation of the primary, which has brightness variation due to inhomogeneous distribution of stellar spots (as the primary star dominates the light in the Kepler bandpass, we assume it is the source of the modulation). To obtain a more precise value of the stellar rotation we measured the lags of the first 12 peaks of the autocorrelation and fitted them with a straight line as shown in Fig. S4. From the slope of the fitted line we derived a value of 7.775 ± 0.022 days as our best value for the stellar rotation period. This period is slightly longer than the orbital period of 7.448 days. It is interesting to note that the transition between synchronized and unsynchronized binaries for pre-main sequence and young stars appears between 7 and 8 days, as depicted by (*27*).

1.4 Spectroscopic observations

We observed Kepler-47 four times with the High-Resolution-Spectrograph (*28,* HRS) at the Hobby-Eberly Telescope (HET). Spectra with a resolving power of $R = 30,000$ were obtained on UT 2012, April 23, May 18 & 20 and June 5. We used the "600g5822" setting of HRS that delivers a spectrum from 4814 to 6793 Å. The data were reduced with our own HRS reduction script using standard IRAF routines. We selected a total exposure of 3600 seconds per spectrum (divided into three sub-exposures of 1200 seconds each to facilitate cosmic-ray removal). The signal-to-noise (S/N) levels of the HRS spectra range from 30:1 to 55:1 at 5500 Å, depending on seeing conditions. Adjacent to every visit to Kepler-47 we also observed the Kepler field standard star HD 182488 to be used for the radial velocity determination.

In addition to the HET observations, we observed Kepler-47 six times using the Tull Coudé spectrograph (*29*) at the Harlan J. Smith 2.7m telescope (HJST). The data were obtained with our standard instrumental setup that covers the a wavelength range of 3760-10,200 Å and uses a 1.2 arcsecond slit that yields a resolving power of $R = 60,000$. We obtained data during the

nights of UT 2012, May 1, 2, 4-6 and on June 26. Exposure times ranged from 3600 to 4800 seconds (again divided in 1200 second sub-exposures) and the S/N is typically around 14:1 at 5500Å. Each of these nights we also observed HD 182488 to serve as a radial velocity standard. The data were reduced with our own reduction scripts using standard IRAF routines. After some experimentation, it was discovered that better measurements of the radial velocities were obtained from spectra that did not have the sky background subtracted.

An additional spectrum of Kepler-47 was obtained using the 10 m Keck 1 telescope and the HIRES spectrograph (*30*). The spectra were collected using the standard planet search setup and reduction (*31*). The resolving power is $R = 60,000$ at 5500 Å. Sky subtraction, using the "C2 decker" was implemented with a slit that projects to 0.87×14.0 arcsec on the sky. The wavelength calibrations were made using Thorium-Argon lamp spectra.

The radial velocities of Kepler-47 were measured using the "broadening function" technique (*32*). The broadening functions (BFs) are rotational broadening kernels, where the centroid of the peak yields the Doppler shift and where the width of the peak is a measure of the rotational broadening. The BF analysis is often better suited for measuring radial velocities of binary stars in cases where the velocity difference between the two stars is small compared to the spectral resolution. A high quality spectrum of a slowly rotating star is needed for the BF analysis, and for this purpose we used observations of HD182488 (spectral type G8V) taken with each telescope+instrument combination. The derived radial velocities are insensitive to the precise spectral type of the template, as similar radial velocities are found when using templates of early G to late K. The adopted template radial velocity was -21.508 km s^{-1} (*33*).

We prepared the spectra for the BF analysis by normalizing each echelle order to the local continuum using cubic splines, trimming the low signal-to-noise ends of each order, and merging the orders by interpolating to a log-linear wavelength scale. The wavelength ranges used for the final BF analysis was 4830-5770 Å for the HET spectra and 5138-5509 Å for the HJST spectra. Fig. S5 shows example BFs from HET and HJST spectra. The spectrum is single-lined, as only one peak is evident in the BFs from the HET. Some simple simulations were performed, and non-detection of a second star in the HET spectra indicates the secondary star is $\gtrsim 10$ times fainter than the primary star, consistent with the expectations based on the eclipse depths, where a flux ratio of $\sim 1/176$ is expected. In the case of the HJST, two peaks are apparent. However, one of the peaks is due to the sky background since it is stationary in velocity, and changes strength relative to the other. The FWHM of the BF peaks were consistent with the instrumental broadening, which indicates the rotational velocity of the primary is at best only marginally resolved.

Gaussian functions were fit to the BF peaks to determine the relative Doppler shifts. The appropriate barycentric velocity corrections were applied and the contribution of the template radial velocity was removed, thereby placing the radial velocities on the standard IAU radial velocity scale defined by (*33*) and (*34*). The Keck HIRES pipeline automatically produces radial measurements for single stars on the IAU scale, accurate to 0.1 km s^{-1} or better (*34*). Having established Kepler-47 as a single-lined binary, we simply adopted the pipeline measurement. The radial velocity measurements for all 11 observations are given in Table S1.

1.5 Spectroscopic parameters

The effective temperature $T_{\rm eff}$, surface gravity $\log g$, the metallicity [m/H], and the rotational velocity $V_{\rm rot} \sin i$ of the primary were measured using the Stellar Parameter Classification (SPC) code (*35*). SPC uses a cross-correlation analysis against a large grid of model spectra in the wavelength region 5050 to 5360 Å. Since all of the absorption lines in this region are used, the SPC analysis is ideal for spectra with low signal-to-noise. The first three HET observations were combined to yield a spectrum with a signal-to-noise ratio of ≈ 116 in the order containing the Mg b features near 5169 Å (the fourth HET observation had relatively high sky contamination and was not used). The derived spectroscopic parameters are given in Table S2.

1.6 Stellar eclipse times and corrections

The times of mid-eclipse for the primary and secondary eclipses in Kepler-47 were measured using the technique described in (*7*). For completeness we give most of the details here as well. Given an initial linear ephemeris and an initial estimate of the eclipse widths, the data near the eclipses were isolated and locally detrended using a cubic polynomial with the eclipses masked out. The detrended data were then folded on the linear ephemeris and an eclipse template was made by fitting a cubic Hermite spline. The Piecewise Cubic Hermite Spline (PCHS) model template was then iteratively cross-correlated with each individual eclipse event to produce a measurement of the time at mid-eclipse. After each iteration, a new PCHS model was produced by using the latest measured times to fold the data. Fig. S6 shows the folded eclipse profiles and the final PCHS models. The fits are generally good, although there is increased scatter near the middle of the primary eclipse, presumably due to the effects of star spots. Table S3 gives the eclipse times. The cycle numbers for the secondary eclipse are not exactly half integers because the orbit is eccentric.

The eclipse times were fitted with a linear ephemeris and the Observed minus Computed (O-C) residual times were calculated and are shown in Fig. S7. For the primary, there are coherent deviations of up to two minutes. While not strictly periodic, there is a quasiperiod of ≈ 178 days seen in a periodogram (Fig. S8). This modulation is most likely a beat frequency between the stellar rotation and the binary motion, similar to what is observed for Kepler-17 (*20*). If the secondary passes in front of a big spot during the primary eclipse, the spot anomaly will introduce a shift on the eclipse timing since the projected stellar disk of the primary on the sky will no longer have a symmetric surface brightness distribution. The shift of the eclipse time will depend on the size and position of the spot and the position on the eclipse chord. A long-lasting spot will introduce shifts in consecutive eclipses, but the shift will change with time since the spot will be at a different position on the eclipse chord at each eclipse. More specifically for this system, a spot with a period of rotation of 7.775 days will effectively recede on the transit chord $360^\circ(7.4484\ d - 7.775\ d)/7.4484\ d = -15.79^\circ$ each eclipse. In order to come back to the exact same position, and hence complete a full cycle in the O-C diagram, $(360^\circ/15.79^\circ)P_{\rm orb} = 22.8P_{\rm orb} = 170$ days will be needed, which is close to the period of the

observed signal. In reality, the spots also change with time and may also drift in latitude over time, so the signal near the beat frequency is blurred somewhat.

There is a correlation between the O-C residual time of the primary eclipse and the local slope of the out-of-eclipse portions of the SAP light curve during the eclipse, as shown in Fig. S9. A large negative slope in the light curve surrounding an eclipse indicates a dark spot is rotating into view. The "center of light" of the primary will be shifted to the opposite side of the stellar disk, resulting in a slightly later time of mid-eclipse. Likewise, a large positive slope surrounding an eclipse indicates a dark spot is rotating out of view, which results in a slightly earlier time of mid-eclipse. Finally, when the slope is near zero, the spots are centered on the stellar disk, and no change in the eclipse time is seen. A linear function was fitted to the data in Fig. S9, and the times of primary eclipse were corrected. The O-C diagram resulting from these corrected times (Fig. S7) has much less scatter. No periodicities are evident (Fig. S8).

The best-fitting ephemerides for the corrected primary eclipse times and the secondary eclipse times are

$$
\begin{array}{rcrl}
P_A & = & 7.44837605 \pm 0.00000050 \text{ d} & \text{Kepler-47 primary} \\
P_B & = & 7.44838227 \pm 0.00000342 \text{ d} & \text{Kepler-47 secondary} \\
T_0(A) & = & 2,454,963.24539 \pm 0.000041 & \text{Kepler-47 primary} \\
T_0(B) & = & 2,454,959.426986 \pm 0.000277 & \text{Kepler-47 secondary}
\end{array}
$$

The difference between the primary and secondary periods is 0.52 ± 0.30 seconds, with the secondary period being longer.

1.7 The effect of star-spots on the eclipses: possible biases and spin-orbit alignment.

Star-spots cause the light curve to exhibit modulations that can be used to measure the rotation period of the primary star. Star-spots can also affect the determination of certain system parameters. It has been shown that there is a correlation between the eclipse timing variations and the local slope of the stellar flux variations at the times of the eclipses. In order to confirm that star-spots are the main cause of the eclipse timing variations, and to evaluate their impact on our ability to measure the size of the secondary star, we attempt to model the effect of spots on individual eclipses (*21,36,37*).

The data from each primary eclipse are isolated by keeping only 3 hours of observations before and after the eclipse. The out-of-eclipse part of each dataset is then fitted with a linear function. The fit is subtracted from the data, then the data are normalized so the out-of-eclipse flux is equal to unity. The detrended eclipse light curves are folded with a linear ephemeris, and this folded light curve is fitted with a standard model for light loss due to a dark body passing in front of a limb darkened star (*38*). This no-spot model has only four free parameters: squared radius ratio $(R_B/R_A)^2$, impact parameter b, normalized semimajor axis for the secondary orbit R_A/a_B, and a linear limb darkening coefficient u_1.

The effect spots have on individual primary eclipses is manifest in two ways: the depth of each eclipse changes since it is measured relative to the changing stellar flux, and the shape of each eclipse is distorted which leads to a shift in the measured mid-eclipse time. Visual inspection of the eclipse residuals shows that this last effect can be well-modeled in most cases by adding just one large star-spot on the surface of the primary star. Since the rotation of the star happens on a longer time-scale than the eclipse itself, we held the position of the star-spot fixed during each individual eclipse. The latitude of the spots cannot be well constrained with single eclipse events, so we fix the position of the spot so that the center of the secondary star trajectory intersects the center of the spot. Our spot model adds five additional parameters: three parameters describe the spot itself – its angular radius, the flux contrast (related to the spot temperature), and the position along the eclipse chord. The fourth parameter is the out-of-eclipse flux, which corrects for the depth variations. Finally, the time of mid-eclipse is free. We set up a pixilated model of the star with a circular spot, in which the flux is calculated as the surface integral of the intensity of the visible hemisphere of the star.

The best-fitting model for several consecutive eclipses is compared with a no-spot model in Fig. S10, showing how the model captures the essential effect of spots on the eclipses. For every eclipse we obtained a new eclipse time, and fitted a linear ephemeris to these times. The scatter was found to be substantially reduced from the initial timings (see Fig. S7, upper panel), by a factor of 30%, which shows that indeed the scatter is due to spots. The improvement on the scatter is similar to the one obtained through the local slope correction, so this serves as a good consistency check.

Our model also estimates the fraction of the star covered by spots at the time of each eclipse. This quantity is not very precise, but can help us estimate the effect of spots on the measurement of the eclipse depth and hence the radius ratio R_A/R_B. We divide the square of the radius ratio from the spot model by each observed local out-of-eclipse flux to mimic the apparent depth that one would obtain by fitting each eclipse individually. The results are plotted in Fig. S11, where one can clearly see how the depth of each eclipse changes with time. The variations seem to have a time-scale similar to the uncorrected eclipse timing variations, which is expected since the scatter in both are due to spots. A variation with the observing season is also apparent, which is a clear indication that there are different levels of Quarterly contamination. With these eclipse depths we can estimate the inferred secondary star radius R_B from each eclipse, using a fixed R_A from Table 1 (see Fig. S11). The values obtained do not have a large scatter, and they all agree within 1σ with the value obtained from the photometric-dynamical model fit. Thus the correction to the secondary star radius because of the presence of spots is not significant, although a slightly smaller radius is favored.

We can also use these spot models to gain information about the obliquity of the system (*18–21, 39*). In Fig. S10 we can clearly see how the spot model shows that a spot is moving backwards with each eclipse, which means that the spot trajectory is contained within the boundaries of the eclipse chord. This backwards movement makes it seem as if the star is rotating backwards (retrograde) very slowly, but this is simply a stroboscopic alias effect. The spot appears to move backwards because the star's rotation period is slightly longer than the

orbital period.

If we assume that the entire trajectory of a spot is contained on the part of the primary star eclipsed by the secondary star then we can estimate the obliquity of the system (*18*) to be smaller than $\arctan(R_B/R_A) \approx 20^\circ$. The obliquity is likely to be smaller since we have detected more than 10 spots receding with different velocities, and these different velocities could be due to spots at different latitudes exhibiting differential rotation. We note that the obliquity of this target will be very hard to measure with the Rossiter-McLaughlin effect (*40*) due to its faintness, so additional investigation of its spots might be the preferred method to further constrain the obliquity.

In principle, we can use the spectroscopic $V_{\rm rot} \sin i$ together with an estimated rotation period and size of the primary star to obtain information on the inclination of the primary star. The spectroscopic observed $V_{\rm rot} \sin i = 4.1 \pm 0.5$ km s^{-1}, while the inferred $V_{\rm rot} = 2\pi R_A/P_{\rm rot} = 6.3 \pm 0.2$ km s^{-1}. This would imply a highly inclined star ($i_s \approx 40^\circ$). Note, however, that the measured value of the rotational velocity is below the resolution of the spectra, so its value should be treated with caution. In addition, differential rotation can make it harder to compare the surface integrated projected rotational velocity $V_{\rm rot} \sin i$ to the equatorial rotational velocity $2\pi R_A/P_{\rm rot}$ (*39*).

1.8 Transit times for the inner and outer planet and the search for additional transits

All of the transits of the outer planet and about half of the transits of the inner planet are evident in the SAP light curves before any detrending. The rest became visible when the data are carefully detrended. A symmetric polynomial "U-function" template with an adjustable width and depth was used to estimate the times of mid-transit and their durations. A cubic polynomial was used to detrend each transit using five different duration windows around the transit, and the best-fitting one was adopted. The fits for each transit were iterated to determine the best-fitting time of mid-transit and the duration. This method worked well in some cases and failed to converge in other cases. In cases where the convergence failed, the time was estimated using an interactive plotting program, and an uncertainty of 30, 60 or 90 minutes was assigned based on the judged quality of the transit. Table S4 gives the measured times and durations and their uncertainties, and the corresponding model times and durations. We note that the measured times and the durations were only used to establish starting models for the photometric-dynamical models described below. The actual (detrended) light curve was modeled directly.

One "orphan" transit occurring about 12 hours after a transit of planet b was noticed in the Q12 data (Fig. S12). This transit cannot be accounted for by either the inner or the outer planet (the intervals between the nearest transits are 0.5 days and 127 days, respectively). To estimate the significance of the orphan event, a model consisting of two Gaussians was fit to the segment of the detrended light curve shown in Fig. S12, which contains 103 data points. The uncertainties on each point were scaled to give $\chi^2_\nu = 1$ for 96 degrees of freedom. The Gaussian in the model at the location of the orphan was replaced by the background level of 1.0 and the

resulting χ^2 value increased to 205.5, giving a formal significance of $\sim 10.5\sigma$.

No other orphan transits with a significance of $> 3\sigma$ were found using visual searches. An automated search algorithm, dubbed the "Quasi-periodic Automated Transit Search" (QATS) was also used to search for additional transits. The QATS algorithm can allow for unequal time intervals between the transit events. For a given trial period for a potential planet, the expected transit duration at each time in the light curve is computed using a circular orbit for the planet. The data are corrected for the different transit durations and shifted to a common phase to increase the signal-to-noise (the correction for the different widths is quite good, provided the planet's orbit is nearly circular). A "periodogram" is constructed by plotting the significance versus the trial period. QATS detected the inner planet at high significance. Unfortunately QATS is very sensitive to detrending errors for longer periods, and in fact did not detect the outer planet. No additional planets with periods shorter than 150 days were detected at the significance level of the inner planet.

Although the overall duty cycle of the data collection by Kepler is quite high, a non-trivial amount of the light curve is occupied by the stellar eclipses, which in the case of Kepler-47 is $\approx 3-6$ times more than it is for Kepler-16, 34, 35, and 38. Although one could in principle find transits during primary and secondary eclipses, in Kepler-47 this is extremely difficult owing to the effects of star-spots. The primary and secondary eclipse durations together are 0.014 in orbital phase, which is 0.104 days. A combined total of 256 primary and secondary eclipses were observed, giving a total of 26.62 days lost for the purposes of transit searches, lowering the duty cycle to 83.8%.

Finally, if the transit is due to another planet in the Kepler-47 system, its radius would be ≈ 4.5 Earth radii. Without more transit events, it is nearly impossible to determine what the orbital period of such a planet would be. If its orbit is more inclined relative to the other planets, it would not necessarily transit the stars near each conjunction. In addition, if there is precession of the orbit, it is possible for sequences of transits to come and go over long time scales. Thus, the orphan transit could in principle belong to a planet in between the inner and outer one, in spite of the lack of other observed transits.

1.9 Photometric-dynamical model

We modeled the Kepler light curve of Kepler-47 using a dynamical model to predict the motions of the planets and stars, and a eclipse/transit model to predict the light curve.

1.9.1 Description of the model

The "photometric-dynamical model" refers to the model that was used to fit the Kepler photometry. This model is analogous to that described in the analyses of KOI-126 (*13*), Kepler-16 (*6*), Kepler-34 and Kepler-35 (*7*), Kepler-36 (*41*), and Kepler-38 (*8*).

Four bodies were involved in this problem; however, the planets' gravitational interaction with the stars and with each other was determined to be observationally negligible. We therefore

assumed the planets to be massless in our model. The motion of the stellar binary was Keplerian and could be predicted analytically. The planets were modeled as orbiting in the two-body potential of the stars. The motion of each planet was determined via a three-body numerical integration. This integration utilized a hierarchical (or Jacobian) coordinate system. In this system, $\mathbf{r_b}$ ($\mathbf{r_c}$) is the position of Planet b (Planet c) relative to the center-of-mass of the stellar binary (which corresponds to the barycenter in this approximation), and $\mathbf{r}_{\rm EB}$ is the position of Star B relative to Star A. The computations are performed in a Cartesian system, although it is convenient to express $\mathbf{r_b}$ ($\mathbf{r_c}$) and $\mathbf{r}_{\rm EB}$ and their time derivatives in terms of osculating Keplerian orbital elements: instantaneous period, eccentricity, argument of pericenter, inclination, longitude of the ascending node, and time of barycentric conjunction: $P_{b,c,\rm EB}$, $e_{b,c,\rm EB}$, $i_{b,c,\rm EB}$, $\omega_{b,c,\rm EB}$, $\Omega_{b,c,\rm EB}$, $T_{b,c,\rm EB}$, respectively. We note that these parameters do not necessarily reflect observables in the light curve; the unique three-body effects make these parameters functions of time (and we refer to these coordinates as "osculating").

The accelerations of the three bodies are determined from Newton's equations of motion, which depend on $\mathbf{r_b}$ ($\mathbf{r_c}$), $\mathbf{r}_{\rm EB}$ and the masses (*42*, *43*). For the purpose of reporting the masses and radii in Solar units, we assumed $GM_{\rm Sun} = 2.959122 \times 10^{-4}$ AU^3 day^{-2} and $R_{\rm Sun} = 0.00465116$ AU. We used a Bulirsch-Stoer algorithm (*44*) to integrate the coupled first-order differential equations for $\dot{\mathbf{r}}_{b,\rm EB}$ and $\mathbf{r}_{b,\rm EB}$.

The spatial coordinates of all four bodies at each observed time are calculated and used as inputs to model the light curve. The computed flux was the sum of the fluxes assigned to Star A, Star B, and a seasonal (being the four "seasons" of the Kepler spacecraft orientation) source of "third light," minus any missing flux due to eclipses or transits (only planetary transits across Star A were computed, those across Star B are not significant in the Kepler data). The loss of light due to eclipses was calculated as follows. All objects were assumed to be spherical. The sum of the fluxes of Star A and Star B was normalized to unity and the flux of Star B was specified relative to that of Star A. The radial brightness profiles of Star A and Star B were modeled with a linear limb-darkening law, i.e., $I(r)/I(0) = 1 - u_1(1 - \sqrt{1 - r^2})$ where r is the projected distance from the center of a given star, normalized to its radius, and u is the linear limb-darkening parameter. The limb darkening coefficient of Star B was fixed (to $u = 0.5$); letting it vary freely resulted in a negligible change to final parameter posterior.

The radial velocity of Star A was computed from the time derivative of the position of Star A along the line of sight (analytically, in this case) and compared to the radial velocity data.

The continuous model is integrated over a 29.4 minutes interval centered on each long cadence sample before being compared to the long cadence Kepler data.

1.9.2 Local detrending of Kepler data

The Kepler light curve ("SAP_FLUX" from the standard fits product) for Kepler-47, spanning twelve Quarters, is reduced to only those data within 0.5–1 day of any primary or secondary eclipse or any transit of either planet. As noted above, some data are missing as a result of observation breaks during Quarterly data transfers or spacecraft safe modes.

Each continuous segment of data has a local cubic correction in time divided into it. The parameters of this polynomial correction are found through an iterative process, as described as follows. In the first step, we masked the eclipses of the stars and the transits of the planets and then performed a robust nonlinear least-squares fit to each continuous segment. The data, having divided out this correction, were then "fit" with the photo-dynamical model by determining the highest likelihood solution from a Markov Chain Monte Carlo simulation. The best-fit model was then divided into the data and the local nonlinear fits were recomputed (this time without masking the eclipses and transits). This process was repeated until the corrections converged to a sufficient tolerance.

1.9.3 Specification of parameters

A reference epoch for the three-body integration was specified for each planet near a particular transit. Those epochs were chosen to be 2,454,969.216 BJD and 2,455,246.6545 BJD for planets b and c, respectively.

The model has 33 adjustable parameters. Two parameters are related to Star A: the stellar density times the gravitational constant, $G\rho_A$, and the stellar mass times G, GM_A. One parameter gives the mass ratio of the stars, $q \equiv M_B/M_A$. Six parameters encode the eccentricities and arguments of pericenter for the planetary and stellar orbits about the barycenter in a way that reduces nonlinear correlations:

$$h_{b,c} \equiv \sqrt{e_{b,c}} \sin \omega_{b,c} \quad \text{(S1)}$$

$$k_{b,c} \equiv \sqrt{e_{b,c}} \cos \omega_{b,c} \quad \text{(S2)}$$

$$H \equiv e_{EB} \sin \omega_{EB} \quad \text{(S3)}$$

$$K \equiv e_{EB} \cos \omega_{EB} \quad \text{(S4)}$$

The remaining osculating parameters, 11 in total, are the periods $P_{b,c}$, P_{EB}, the orbital inclinations $i_{b,c}$, i_{EB}, the times of conjunction with barycenter, $T_{b,c}$, T_{EB} and the difference between the nodal longitudes of the planets to that of the stellar binary $\Delta\Omega_{b,c}$. The absolute nodal angle relative to North of the stellar binary cannot be determined and was fixed to zero in practice.

Three more parameters are the relative radii of Star B and the planets to that of Star A: $r_B \equiv R_B/R_A$ and $r_{b,c} \equiv R_{b,c}/R_A$. One parameter, u, parameterizes the linear limb darkening law for Star A (described above). Another parameter gives the relative flux contribution of Star B, F_B/F_A.

A single parameter, $\sigma_{\rm LC}$, describes the width of the probability distribution for the photometric noise of the long cadence observations, assumed to be stationary, white and Gaussian-distributed.

Three parameters characterize the radial velocity measurements: the constant offset of the radial velocity, γ, the offset between the HET and HJST velocities, $\Delta\gamma$, and a "stellar jitter" term, σ_{RV}, which contributes to the measured errors for each radial velocity observation, in

quadrature. Because only one Keck observation was made, this radial velocity could not be offset to match the HET and HJST velocities in a sensible way, and therefore was omitted in the modeling.

Additionally, we specify 4 more parameters describing the relative extra flux summed in the aperture. The four parameters specify the constant extra flux in each Kepler "season." The Kepler spacecraft is in one of four orientations during a year; a constant level of "third light" is assumed for all Quarters sharing a common season.

1.9.4 Priors and likelihood

We assumed uniform priors for all 33 parameters. For the eccentricity parameters, this corresponds to uniform priors in $e_{b,c}$ and $\omega_{b,c}$, but a prior that scales as e_{EB} for the stellar eccentricity. This eccentricity is sufficiently determined that this non-uniform prior does not dominate the posterior distribution.

The likelihood $\mathcal{L}$ of a given set of parameters was taken to be the product of likelihoods based on the photometric data and radial velocity data:

$$\begin{aligned} \mathcal{L} \quad \propto \quad & \sigma_{\rm LC}^{-N_{\rm LC}} \exp\left[-\sum_{i}^{N_{\rm LC}} \frac{(\Delta F_i^{LC})^2}{2\sigma_{\rm LC}^2}\right] \\ & \times \prod_{j}^{N_{\rm RV}} \left(\sigma_j^2 + \sigma_{RV}^2\right)^{-1/2} \exp\left[-\frac{(\Delta V_j)^2}{2\left(\sigma_j^2 + \sigma_{RV}^2\right)}\right] \end{aligned} \tag{S5}$$

where $\Delta F_i^{\rm LC}$ is the ith photometric data residual, $\sigma_{\rm LC}$ is the width parameter describing the photometric noise of the long cadence data, ΔV_j is the jth radial velocity residual, σ_j is the uncertainty in the jth radial velocity measurement and σ_{RV} is the stellar jitter term added in quadrature with the σ_j.

1.9.5 Best-fit model

We determined the best-fit model by maximizing the likelihood. The maximum likelihood solution was found by finding the highest likelihood in a large draw from the posterior as simulated with a Markov Chain Monte Carlo simulation as described below. Fig. S13 shows 18 transits of the inner planet, and Fig. S14 shows the residuals (observed data minus the model). With a few exceptions, there are no strong patterns in the residuals. Fig. S15 shows the model fits and the residuals for the outer planet. There are no patterns evident in the residuals. The residuals for the fits to the primary eclipses are shown in Fig. S16 and the residuals for the fits to the secondary eclipses are shown in Fig. S17. Spot crossing events are evident in many of the primary eclipses. Fig. S18 shows the radial velocity measurements and the best-fitting model and the residuals of the fit. Generally the absolute value of the radial velocity residuals is less than about 200 m s^{-1}.

The photometric noise parameter, σ_{LC}, has a best-fit value of $\sigma_{LC} = 629.5$ ppm. For comparison, the root-mean-square deviation of the best-fit residuals is 626.9 ppm. This is similar to the expected noise in the light curve of 635 ppm as estimated using an on-line tool provided by the Kepler Guest Observer Office[1], where we used an apparent magnitude of Kp=15.18 and 20 pixels in the aperture. For this σ_{LC}, the χ^2-metric for the photometric data is $\chi^2 = 10576$ with 10629 degrees of freedom. If we fail to include planet b in our model (by setting its radius to zero), the χ^2 increases by $\Delta\chi^2 = 343.4$. If we ignore planet c, the χ^2 increases by $\Delta\chi^2 = 248.2$.

The stellar jitter parameter, σ_{RV}, has a best-fit value of $\sigma_{RV} = 0.31$ km s^{-1}. The value of χ^2 for the radial velocity data alone is $\chi^2 = 8.85$ for the 10 radial velocity observations.

Fig. S19 shows schematic diagrams of the Kepler-47 orbits. The projected orbits of planets b and c cross the projected disk of the primary, and so transits of both planets across the primary occur, as do occultations of both planets by star A. The former events are observed, whereas the latter events are not observable given the noise level. On the other hand, owing to its small radius, the projected disk of star B does not intersect the projected orbits of the planets, and as such no transits of star B or occultations due to star B occur for the best-fitting orbital configuration. Due to the uncertainties in the relative nodal angles, transits of the planets across star B might occur for a subset of the acceptable solutions. However, even if transits across star B did occur, the expected transit depth would be ~ 30 times weaker than the transits across the primary, and would not be observable in the light curve given the noise level.

1.9.6 Parameter estimation methodology

We explored the parameter space and estimated the posterior parameter distribution with a Differential Evolution Markov Chain Monte Carlo (DE-MCMC) algorithm (*45*).

We generated a population of 100 chains and evolved them through approximately 200,000 generations. The initial parameter states of the 100 chains were randomly selected from an overdispersed region in parameter space bounding the final posterior distribution. The first 10% of the links in each individual Markov chain were clipped, and the resulting chains were concatenated to form a single Markov chain, after having confirmed that each chain had converged according to the standard criteria.

The parameter values and derived values reported in Tables S5 and S6 beside the best-fit values (see above), were found by computing the 15.8%, 50%, 84.2% levels of the cumulative distribution of the marginalized posterior for each parameter. Figure S20 shows two-parameter joint distributions between all parameters. This figure is meant to highlight the qualitative features of the posterior as opposed to providing quantitative ranges. The numbers in that figure correspond to the model parameters in Table S5 with the same number listed as in the first column, if available.

Figures S21 and S22 show the posterior distribution in the eccentricity and argument of pericenter planes The distribution of the three-dimensional inclination between the planets'

[1]http://keplergo.arc.nasa.gov/CalibrationSN.shtml

orbits and the invariable plane is shown in Figure S23.

1.9.7 Predicted ephemerides and transit parameters

Tables S7 and S8 provide the predicted times of transit, impact parameters, normalized transit velocities and durations over 7 years, starting with Kepler Quarter Q13.

1.10 ELC light curve models

Although the secondary star is not detected spectroscopically, its temperature can be estimated using the temperature of the primary derived using SPC, and the temperature ratio derived from modeling the eclipses. In order to find the temperature ratio, and to have an independent check on the results from the photometric-dynamical model, we modeled the light and velocity curves using the Eclipsing Light Curve (ELC) code (*46*) with its genetic algorithm and Monte Carlo Markov Chain optimizers. The free parameters include the temperature ratio T_B/T_A, the primary's limb darkening parameters x_A and y_A for the quadratic limb darkening law [$I(\mu) = I_0(1 - x(1 - \mu) - y(1 - \mu)^2)$], the orbital parameters (e, ω, i), and the fractional radii R_A/a and R_B/a. The stellar masses and the orbital period were held fixed at the values derived from the photometric-dynamical model discussed above.

In ELC, the shapes of the stars are computed using a "Roche" potential modified to account for nonsynchronous rotation and eccentric orbits (*47*,*48*). Given the mass ratio and the fractional radii, the volumes of each star are found by numerical integration. The effective radius of each star is taken to be the radius of a sphere with the same volume as the equipotential surface. In the case of Kepler-47, the stars are very nearly spherical. For the primary at periastron, the ratio of the polar radius to its effective radius is 0.99988, and the ratio of the radius along the line of centers to the effective radius is 1.00007. The amplitude of the out-of-eclipse modulation in the light curve due to ellipsoidal variations, reflection, and Doppler boosting is on the order of 400 ppm, which is ≈ 75 times smaller than the modulation due to star-spots. Thus the use of spherical stars in the photometric-dynamical model is a very good approximation.

Since the numerical integrations are very CPU intensive, ELC has a fast "analytic" mode where the equations given in (*49*) are used. The normalized light curve was divided into 41 segments containing two or three pairs of primary and secondary eclipses. These segments were modeled separately in order to help assess the systematic errors associated with the changing star-spots and the changes in the contamination from Quarter to Quarter. For each fitting parameter, we computed the mean of the best-fitting values and the standard deviation. Table S9 gives the mean values and standard deviations, which we adopt as 1σ errors.

Based on the temperature of the primary derived from the SPC analysis, and the temperature ratio found from the ELC models, we derive a temperature of 3357 ± 100 K for the secondary.

1.11 Upper limits on planetary masses

Upper limits on the masses of the planets can be placed separately as follows. The mass of the inner planet is best constrained by the lack of eclipse timing variations due to gravitational perturbations from that planet. The planet will induce short-term eclipse timing variations with a period equal to the planet's period. It will also cause precession of the binary. Over the timescale of a few years, the binary precession will cause a slight change in the phase difference between the primary and secondary eclipses, which can be observed as a slight difference between the primary and secondary eclipse periods. Numerical simulations showed that in this case the stronger upper limit comes from the lack of short-term eclipse timing variations. A grid of masses for the inner planet was used, and equations of motion for a three body system were integrated, holding the orbital parameters of the binary at their best-fitting values (the nature of the perturbations on the binary are insensitive to anything except the planet's mass). The period and epoch of the binary was found, and the predicted times of eclipse were compared to the measured times. The χ^2 value changes smoothly with the planet's mass, and going to $\chi^2 = \chi^2_{\rm min} + 9$ gives a 3σ upper limit of 2.7 Jupiter masses for the uncorrected eclipse times and 2.0 Jupiter masses for the eclipse times corrected for the effect of star-spots. We adopt the latter value as the 3σ upper limit on the mass of the inner planet.

The mass of the outer planet was best constrained by light travel time (LTT) effects. We fit an LTT orbit to the corrected eclipse times, using a period of 303.13 days and constraining the eccentricity to be $e < 0.2$. While no convincing signal is seen at that period, the best-fitting orbit formally has a semiamplitude of 3.84 ± 1.84 seconds. Given the total mass of the binary and the period of the outer planet, we find a 3σ upper mass limit of 28 Jupiter masses.

1.12 Stability of orbits and limits on eccentricity

We carried out an extensive study of the dynamics of the system and its long-term stability. The orbits of the two planets were integrated, numerically, for different values of their masses and orbital eccentricities. To determine an upper limit for the eccentricity of planet c, we held constant all orbital elements at their best-fit values and integrated the system varying the eccentricity of this planet. Results indicated that the system maintained stability for at least 100 Myr and for $e_c < 0.6$. An examination of the semimajor axis, eccentricity, and orbital inclination of each planet during the course of the integrations showed that the variations of these quantities were negligibly small, supporting the idea that the two planets do not disturb each other's orbits. The results stayed unchanged when the masses of the two planets were increased to 0.21 and 0.63 Jupiter masses, roughly ten times their plausible values based on the empirical mass-radius relations (*14*, *15*).

Both the photometric-dynamical model and stability simulations used a Newtonian 4-body numerical integrator. A more physical model would include the precession of the binary due to general relativity (GR) and the tidal and rotational bulges. Expressions for the rate of precession due to these effects (*50*) show that GR dominates, and it would cause a full periastron rotation

in ~ 6700 years. In the current observations, such precession would cause the period of primary and secondary eclipse to differ fractionally by $\sim 10^{-7}$, whereas the uncertainty of this quantity is 4.6×10^{-7}. The GR precession period is much longer than the periastron period of the planets – e.g., numerical integrations of planet c showing a ~ 560 year precession cycle due to the effective quadrupolar gravitational potential of the binary – so it has little dynamical importance. Therefore GR and other precession effects are neither detectable nor significantly change our assessment of stability, so GR has little dynamical importance.

1.13 Comparison with stellar evolution models

The reasonably precise absolute dimensions determined for the stars in Kepler-47 (4–5% relative errors for the masses, and 1.8% for the radii) offer an opportunity to compare the measurements with models of stellar evolution. This is of particular interest for the late M-dwarf secondary, given that low-mass stars have shown discrepancies with theory in the sense that they are generally larger and cooler than predicted. These anomalies are believed to be due to stellar activity (*51, 52*).

In Fig. S24 we compare the measurements for the primary star with a stellar evolution track from the Yonsei-Yale series (*53, 54*), interpolated to the exact mass we measure. The metallicity of this model is set by our spectroscopic determination of $[\mathrm{Fe/H}] = -0.25$, where we assume the iron abundance tracks the metallicity measurement from SPC. The model is consistent with the observations to within less than 2σ, and the small difference may be due either to slightly biased spectroscopic parameters (temperature and metallicity) or a slightly overestimated mass for the primary star. As a check, we produced a photometric estimate of the temperature using available photometry from the KIC and empirical color-temperature calibrations along with the reddening listed in the KIC. The result suggests a value closer to 5900 K than 5600 K, although we consider this evidence to be somewhat circumstantial and highly dependent on reddening. We confirmed that the level of agreement between theory and observation is independent of the adopted model physics by comparing the primary star parameters with BaSTI stellar evolutionary tracks (*55*), which yielded similar results as the Yonsei-Yale models.

In Fig. S25 we compare the measurements for both components against models from the Dartmouth series (*56*), which incorporate physical ingredients (equation of state, non-grey boundary conditions) more appropriate for low-mass stars. We find the radius of the secondary of Kepler-47 to be consistent with these models, which would be an exception to the general trend mentioned above, although the mass error is large enough ($\sim$4%) that the conclusion is not as strong as in other cases. Its temperature, however, is lower than predicted for a star of this mass by about 200 K. This deviation is in the same direction as seen for other low-mass stars. Because the secondary is so faint, we have no information on its activity level. Age estimates for the system from this figure and the previous one are somewhat conflicting, and only allow us to say that Kepler-47 is very roughly of solar age.

1.14 Details of habitable zone

To determine the insolation limits of the habitable zone for Kepler-47 c, we follow the relations given by (*24*) that include the stellar temperature as well as luminosity. The temperature term accounts for the different relative amount of infrared flux to total flux, which is important for atmospheric heating. We use the criteria of a runaway greenhouse effect for the inner boundary and the maximum greenhouse effect for a cloud-free carbon dioxide atmosphere for the outer boundary. This is more conservative than the "recent Venus" and "early Mars" criteria, but less conservative than the "water loss" and "first carbon dioxide condensation" criteria (*24*). The secondary star emits only 1.7% as much energy as the primary star (and only 0.58% in the Kepler bandpass), so its contribution is neglected. The resulting insolation limits are shown as the dotted lines in Figure 3 (main text). The relations given in (*57*), i.e. a cloud-free atmosphere yield nearly identical limits.

The average insolation for Kepler-47 c for a circular orbit is 87% of the Sun-Earth insolation, and varies by $\sim 9\%$ peak-to-peak. For an eccentricity of 0.2 the mean insolation is 89% and varies from 59% to 144% of the Sun-Earth value; for an eccentricity of 0.4, the mean is 96% and varies from 43% to 261%. Even in this latter case, which is ruled out at the 95% confidence level by the photometric-dynamical model, the mean is less than the Sun-Earth value, and it is the mean insolation that is most relevant for habitability (*58*). Thus for all allowed eccentricities, Kepler-47 c lies in the habitable zone.

Because the primary star dominates the system both in luminosity and mass (so the primary star remains near the barycenter), the variation in insolation is relatively small for a circular planetary orbit. This is seen in the upper left panel of Figure 3, where the variations are caused by the 7.4-day orbit of the primary star. For large eccentricities, the variation in insolation are dominated by the non-circular orbit of the planet.

It must be stressed that the habitable zone is defined such that liquid water could persist for a biologically significant time period on an Earth-like planet (i.e. with a terrestrial $CO_2/H_2O/N_2$ atmosphere, plate tectonics, etc.), and the formulations of (*17, 24, 57*) explicitly assume such conditions. For Kepler-47 c these conditions are not met. Nevertheless, the main point is that Kepler-47 c receives approximately the same amount of energy from its stars that the Earth receives from the Sun.

While it neglects most atmospheric physics, the equilibrium temperature T_{eq} of the planet is still a useful characterization. Assuming that the entire surface of the planet radiates isothermally (i.e. the stellar insolation is efficiently advected around the planet), and for a Bond albedo of A_B=0.7, appropriate for a Neptune-size planet and 1 Sun-Earth insolation (*59*), a value of $T_{eq} \sim 200\ K$ is found for eccentricities from 0.0 to 0.3. For A_B=0.34, corresponding to the albedos of Jupiter and Saturn, $T_{eq} \sim 243\ K$. For an Earth-like albedo of 0.29, which is appropriate for a habitable-zone planet, $T_{eq} \sim 247\ K$. The greenhouse effect will lead to temperatures at the 1-bar pressure level that are higher by several tens of degrees.

References and Notes

1. D. G. Koch *et al*., Kepler mission design, realized photometric performance, and early science. *Astrophys. J.* **713**, L79 (2010). doi:10.1088/2041-8205/713/2/L79

2. W. J. Borucki *et al*., Kepler planet-detection mission: Introduction and first results. *Science* **327**, 977 (2010). doi:10.1126/science.1185402 Medline

3. N. M. Batalha *et al*., Planetary candidates observed by Kepler, III: Analysis of the first 16 months of data. *Astrophys. J. Suppl. Ser.* submitted, arXiv1202.5852 (2012).

4. A. Prša *et al*., *Kepler* eclipsing binary stars. I. catalog and principal characterization of 1879 eclipsing binaries in the first data release. *Astron. J.* **141**, 83 (2011). doi:10.1088/0004-6256/141/3/83

5. R. W. Slawson *et al*., *Kepler* eclipsing binary stars. II. 2165 eclipsing binaries in the second data release. *Astron. J.* **142**, 160 (2011). doi:10.1088/0004-6256/142/5/160

6. L. R. Doyle *et al*., Kepler-16: A transiting circumbinary planet. *Science* **333**, 1602 (2011). doi:10.1126/science.1210923 Medline

7. W. F. Welsh *et al*., Transiting circumbinary planets Kepler-34 b and Kepler-35 b. *Nature* **481**, 475 (2012). doi:10.1038/nature10768 Medline

8. J. A. Orosz, W. F. Welsh, J. A. Carter, E. Brugamyer, L. A., Buchhave, et al., The Neptune-sized circumbinary planet Kepler-38b. *Astrophys. J.* in press, arXiv:1208.3712 (2012).

9. S. Meschiari, Circumbinary planet formation in the Kepler-16 system. I. N-body simulations. *Astrophys. J.* **752**, 71 (2012). doi:10.1088/0004-637X/752/1/71

10. S.-J. Paardekooper, Z. M. Leinhardt, P. Thébault, C. Baruteau, How not to build Tatooine: The difficulty of in situ formation of circumbinary planets Kepler 16b, Kepler 34b, and Kepler 35b. *Astrophys. J.* **754**, L16 (2012). doi:10.1088/2041-8205/754/1/L16

11. T. Borkovits, B. Érdi, E. Forgács-Dajka, T. Kovács, On the detectability of long period perturbations in close hierarchical triple stellar systems. *Astron. Astrophys.* **398**, 1091 (2003). doi:10.1051/0004-6361:20021688

12. See the Supplementary Materials on *Science* Online.

13. J. A. Carter *et al*., KOI-126: A triply eclipsing hierarchical triple with two low-mass stars. *Science* **331**, 562 (2011). doi:10.1126/science.1201274 Medline

14. S. R. Kane, D. M. Gelino, The habitable zone gallery. *Publ. Astron. Soc. Pac.* **124**, 323 (2012). doi:10.1086/665271

15. J. J. Lissauer *et al*., Architecture and dynamics of Kepler's candidate multiple transiting planet systems. *Astrophys. J. Suppl. Ser.* **197**, 8 (2011). doi:10.1088/0067-0049/197/1/8

16. M. J. Holman, P. A. Wiegert, Long-term stability of planets in binary systems. *Astron. J.* **117**, 621 (1999). doi:10.1086/300695

17. J. F. Kasting, D. P. Whitmire, R. T. Reynolds, Habitable zones around main sequence stars. *Icarus* **101**, 108 (1993). doi:10.1006/icar.1993.1010 Medline

18. R. Sanchis-Ojeda *et al*., Starspots and spin-orbit alignment in the WASP-4 exoplanetary system. *Astrophys. J.* **733**, 127 (2011). doi:10.1088/0004-637X/733/2/127

19. P. A. Nutzman, D. C. Fabrycky, J. J. Fortney, Using star spots to measure the spin-orbit alignment of transiting planets. *Astrophys. J.* **740**, L10 (2011). doi:10.1088/2041-8205/740/1/L10

20. J. M. Désert *et al*., The hot-Jupiter Kepler-17b: Discovery, obliquity from stroboscopic starspots, and atmospheric characterization. *Astrophys. J. Suppl. Ser.* **197**, 14 (2011). doi:10.1088/0067-0049/197/1/14

21. R. Sanchis-Ojeda *et al*., Alignment of the stellar spin with the orbits of a three-planet system. *Nature* **487**, 449 (2012). doi:10.1038/nature11301 Medline

22. A. Pierens, R. P. Nelson, On the formation and migration of giant planets in circumbinary discs. *Astron. Astrophys.* **483**, 633 (2008). doi:10.1051/0004-6361:200809453

23. A. N. Youdin, K. M. Kratter, S. J. Kenyon, Circumbinary Chaos: Using Pluto's Newest Moon to Constrain the Masses of Nix and Hydra. *Astrophys. J.* **755**, 17 (2012). doi:10.1088/0004-637X/755/1/17

24. D. R. Underwood, B. W. Jones, P. N. Sleep, The evolution of habitable zones during stellar lifetimes and its implications on the search for extraterrestrial life. *Int. J. Astrobiol.* **2**, 289 (2003). doi:10.1017/S1473550404001715

25. T. M. Brown, D. W. Latham, M. E. Everett, G. A. Esquerdo, Kepler input catalog: Photometric calibration and stellar classification. *Astron. J.* **142**, 112 (2011). doi:10.1088/0004-6256/142/4/112

26. K. Kinemuchi *et al*., Demystifying Kepler data: A primer for systematic artifact mitigation. *Publ. Astron. Soc. Pac.* in press, arXiv1207.3093 (2012).

27. T. Mazeh, in Observational Evidence for Tidal Interaction in Close Binary Systems, eds. M.-J. Goupil & J.-P. Zahn, EAS Publications Series, vol. 29, p. 29 (2008).

28. R. G. Tull, High-resolution fiber-coupled spectrograph of the Hobby-Eberly Telescope. *Proc. Soc. Photo-opt. Inst. Eng.* **3355**, 387 (1998).

29. R. G. Tull, P. J. MacQueen, C. Sneden, D. L. Lambert, The high-resolution crossdispersed echelle white-pupil spectrometer of the McDonald Observatory 2.7-m telescope. *Publ. Astron. Soc. Pac.* **107**, 251 (1995). doi:10.1086/133548

30. S. S. Vogt *et al*., HIRES: The highresolution echelle spectrometer on the Keck 10-m Telescope. *Proc. Soc. Photo-opt. Inst. Eng.* **2198**, 362 (1994).

31. G. W. Marcy *et al*., Exoplanet properties from Lick, Keck and AAT. *Phys. Scr.* **T130**, 014001 (2008). doi:10.1088/0031-8949/2008/T130/014001

32. S. M. Rucinski, Spectral-line broadening functions of WUMa-type binaries. I - AW UMa. *Astron. J.* **104**, 1968 (1992). doi:10.1086/116372

33. D. L. Nidever, G. W. Marcy, R. P. Butler, D. A. Fischer, S. S. Vogt, Radial velocities for 889 late-type stars. *Astrophys. J. Suppl. Ser.* **141**, 503 (2002). doi:10.1086/340570

34. C. Chubak, G. W. Marcy, D. A. Fischer, A. W. Howard, H. Isaacson, H., et al., Precise radial velocities of 2046 nearby FGKM stars and 131 standards. *Astrophys. J. Supp. Ser.* submitted, arXiv:1207.6212v1 (2012).

35. L. A. Buchhave *et al*., An abundance of small exoplanets around stars with a wide range of metallicities. *Nature* **486**, 375 (2012). Medline

36. S. Czesla, K. F. Huber, U. Wolter, S. Schröter, J. H. M. M. Schmitt, How stellar activity affects the size estimates of extrasolar planets. *Astron. Astrophys.* **505**, 1277 (2009). doi:10.1051/0004-6361/200912454

37. J. A. Carter *et al*., The transit light curve project. XIII. Sixteen transits of the Super-Earth GJ 1214b. *Astrophys. J.* **730**, 82 (2011). doi:10.1088/0004-637X/730/2/82

38. K. Mandel, E. Agol, Analytic light curves for planetary transit searches. *Astrophys. J.* **580**, L171 (2002). doi:10.1086/345520

39. T. Hirano *et al*., Measurements of stellar inclinations for Kepler planet candidates. *Astrophys. J.* **756**, 66 (2012). doi:10.1088/0004-637X/756/1/66

40. J. N. Winn *et al*., Measurement of spin-orbit alignment in an extrasolar planetary system. *Astrophys. J.* **631**, 1215 (2005). doi:10.1086/432571

41. J. A. Carter *et al*., Kepler-36: A pair of planets with neighboring orbits and dissimilar densities. *Science* **337**, 556 (2012). doi:10.1126/science.1223269 Medline

42. S. Soderhjelm, Third-order and tidal effects in the stellar three-body problem. *Astron. Astrophys.* **141**, 232 (1984).

43. R. A. Mardling, D. N. C. Lin, Calculating the tidal, spin, and dynamical evolution of extrasolar planetary systems. *Astrophys. J.* **573**, 829 (2002). doi:10.1086/340752

44. W. H. Press, S. A. Teukolsky, W. T. Vetterling, B. P. Flannery, Numerical recipes in C++: the art of scientific computing. (Cambridge University Press, Cambridge, 2002).

45. C. J. F. Ter Braak, A Markov Chain Monte Carlo version of the genetic algorithm Differential Evolution: Easy Bayesian computing for real parameter spaces. *Stat. Comput.* **16**, 239 (2006). doi:10.1007/s11222-006-8769-1

46. J. A. Orosz, P. H. Hauschildt, The use of the NextGen model atmospheres for cool giants in a light curve synthesis code. *Astron. Astrophys.* **364**, 265 (2000).

47. Y. Avni, The eclipse duration of the X-ray pulsar 3U 0900-40. *Astrophys. J.* **209**, 574 (1976). doi:10.1086/154752

48. R. E. Wilson, Eccentric orbit generalization and simultaneous solution of binary star light and velocity curves. *Astrophys. J.* **234**, 1054 (1979). doi:10.1086/157588

49. A. Giménez, Equations for the analysis of the light curves of extra-solar planetary transits. *Astron. Astrophys.* **450**, 1231 (2006). doi:10.1051/0004-6361:20054445

50. D. Fabrycky, Non-Keplerian dynamics of exoplanets. in Exoplanets. ed. S. Seager, University of Arizona Press, p. 217 (2011).

51. M. López-Morales, On the correlation between the magnetic activity levels, metallicities, and radii of low-mass stars. *Astrophys. J.* **660**, 732 (2007). doi:10.1086/513142

52. G. Torres, J. Andersen, A. Giménez, Accurate masses and radii of normal stars: Modern results and applications. *Astron. Astrophys. Rev.* **18**, 67 (2010). doi:10.1007/s00159-009-0025-1

53. S. Yi *et al*., Toward better age estimates for stellar populations: The Y2 isochrones for solar mixture. *Astrophys. J. Suppl. Ser.* **136**, 417 (2001). doi:10.1086/321795

54. P. Demarque, J. H. Woo, Y.-C. Kim, S. K. Yi, Y2 Isochrones with an improved core overshoot treatment. *Astrophys. J. Suppl. Ser.* **155**, 667 (2004). doi:10.1086/424966

55. A. Pietrinferni, S. Cassisi, M. Salaris, F. Castelli, A large stellar evolution database for population synthesis studies. I. scaled solar models and isochrones. *Astrophys. J.* **612**, 168 (2004). doi:10.1086/422498

56. A. Dotter *et al*., The Dartmouth stellar evolution database. *Astrophys. J. Suppl. Ser.* **178**, 89 (2008). doi:10.1086/589654

57. F. Selsis *et al*., Habitable planets around the star Gliese 581? *Astron. Astrophys.* **476**, 1373 (2007). doi:10.1051/0004-6361:20078091

58. D. M. Williams, D. Pollard, Earth-like worlds on eccentric orbits: Excursions beyond the habitable zone. *Int. J. Astrobiol.* **1**, 61 (2002). doi:10.1017/S1473550402001064

59. K. L. Cahoy, M. S. Marley, J. J. Fortney, Exoplanet albedo spectra and colors as a function of planet phase, separation, and metallicity. *Astrophys. J.* **724**, 189 (2010). doi:10.1088/0004-637X/724/1/189

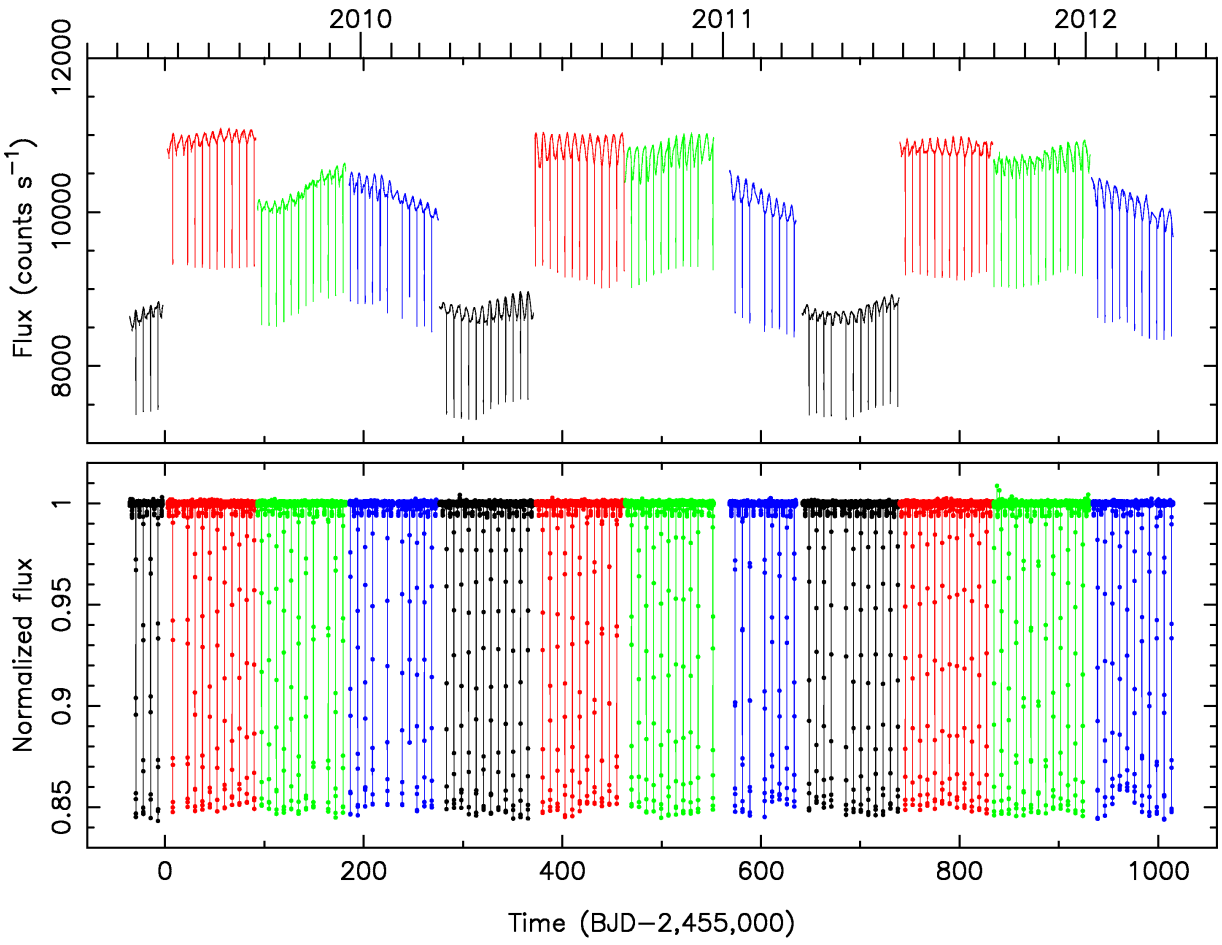

Figure S1: **SAP and detrended light curves.** Top: The SAP light curves of Kepler-47 are shown. The colors denote the season and hence the spacecraft orientation where black is for Q1, Q5, and Q9, red is for Q2, Q6, and Q10, green is for Q3, Q7, and Q11, and blue is for Q4, Q8, and Q12. Bottom: The normalized and detrended light curve with the spot modulation removed is shown. Fifteen primary eclipses and thirteen secondary eclipses were missed during monthly data downloads, spacecraft rolls between Quarters, spacecraft safe modes, and interruptions caused by solar flares.

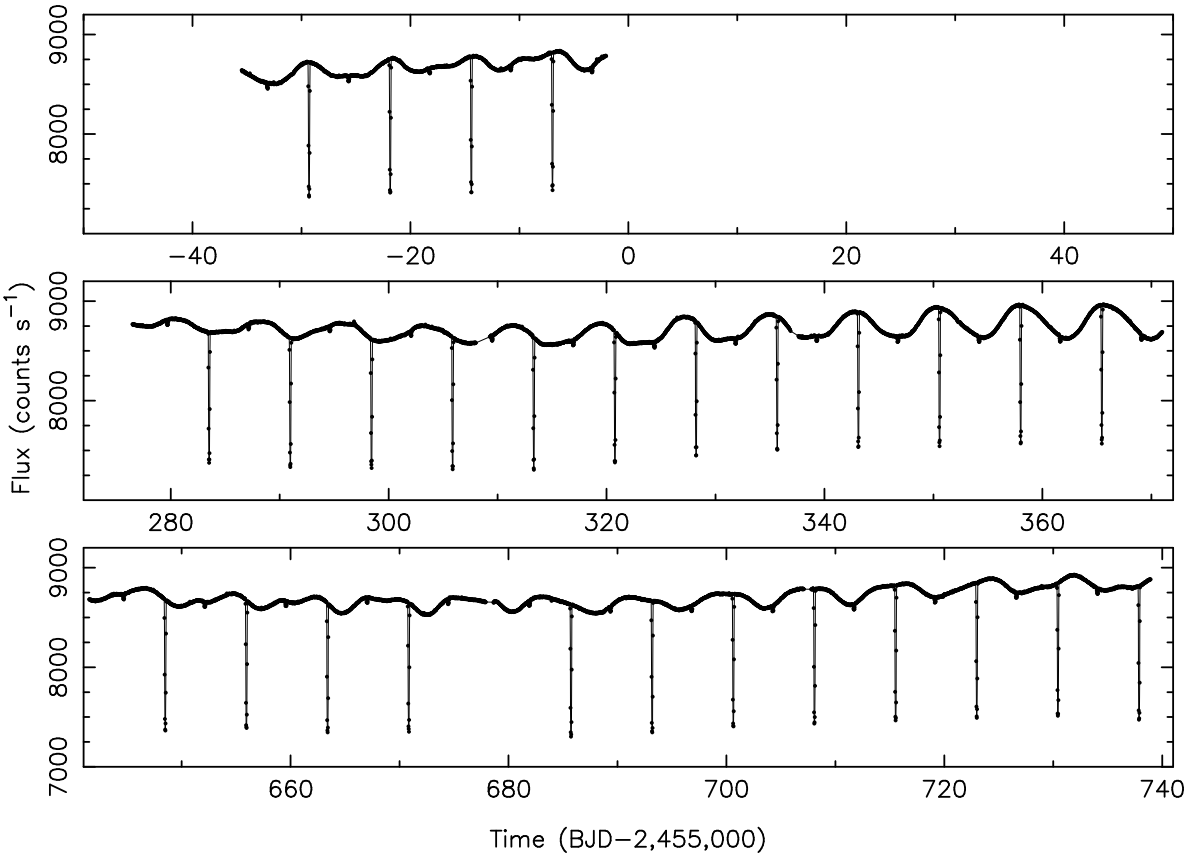

Figure S2: **Light curves showing spot modulations.** The SAP light curves of Kepler-47 from Q1 (top), Q5 (middle), and Q9 (bottom) are shown. The target appeared on the same detector module during these Quarters. A modulation in the out-of-eclipse regions due to star spots is evident.

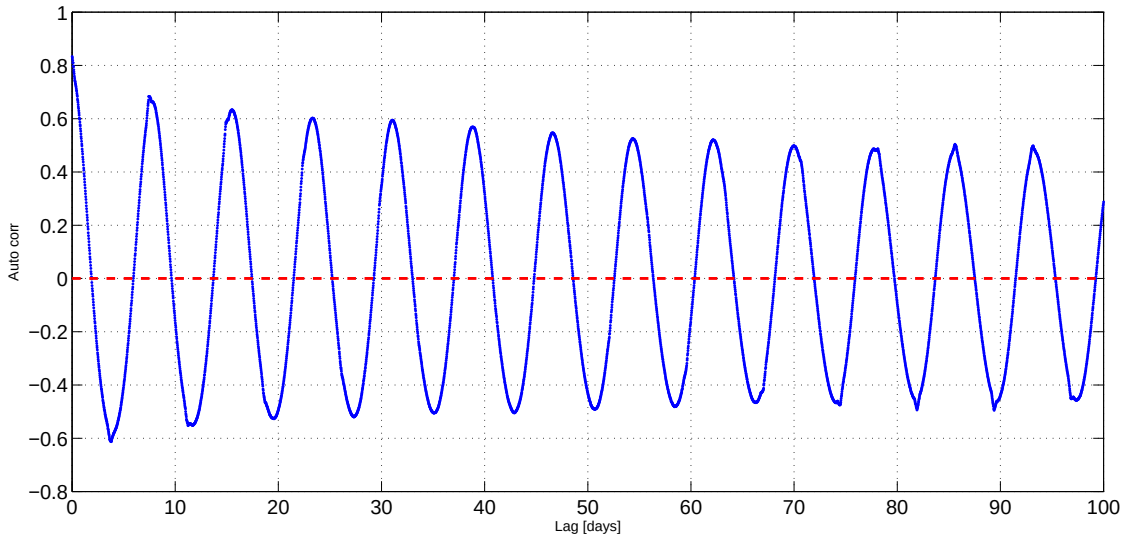

Figure S3: **The autocorrelation function of the cleaned light curve with the eclipses removed.**

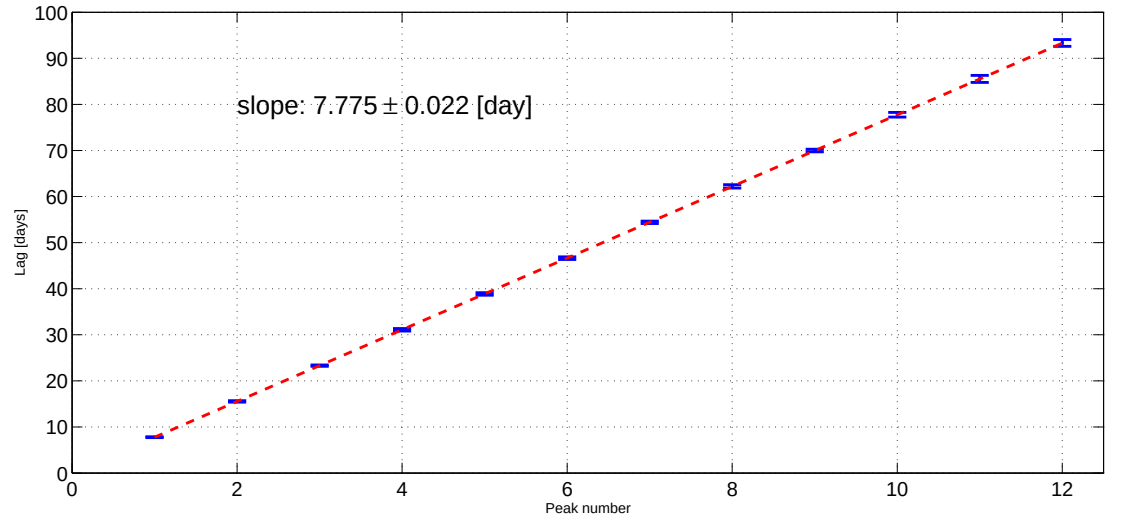

Figure S4: **The measured lag versus the peak number in the autocorrelation function.** The measured lag of the peaks in the autocorrelation function displayed in Fig. S3 is shown. The dashed line is a linear fit to these points. The slope of 7.775 ± 0.022 days is taken to be the rotation period of the primary star.

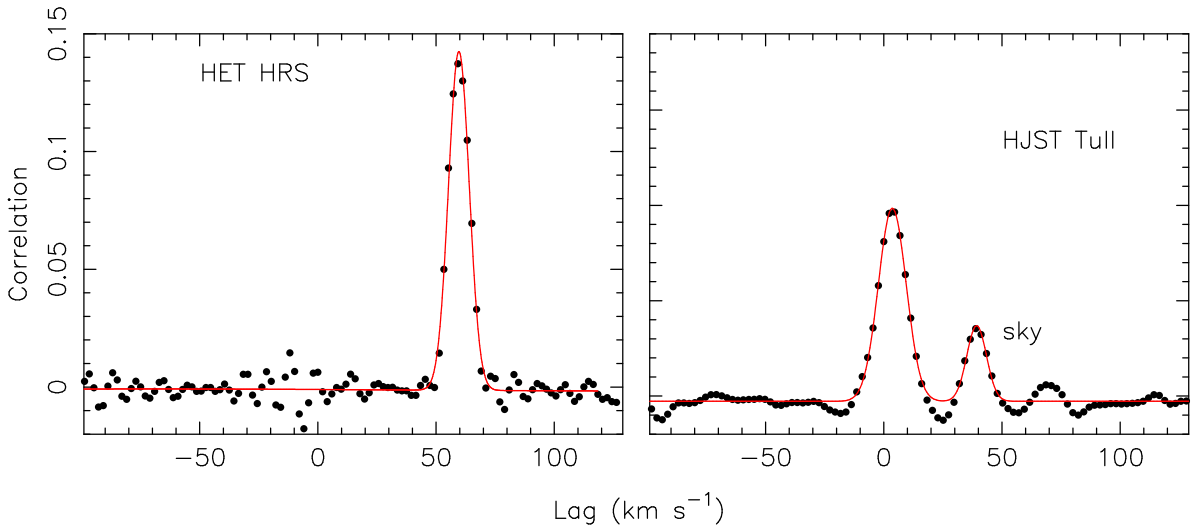

Figure S5: **Representative broadening functions.** Broadening functions (BFs) from the HET+HRS (left) and the HJST+Tull spectrograph (right) are shown. The solid lines are the best-fitting Gaussians. The smaller peak in the HJST BF is due to the sky background. In all cases, the BF peak due to the sky was resolved from the object BF peak.

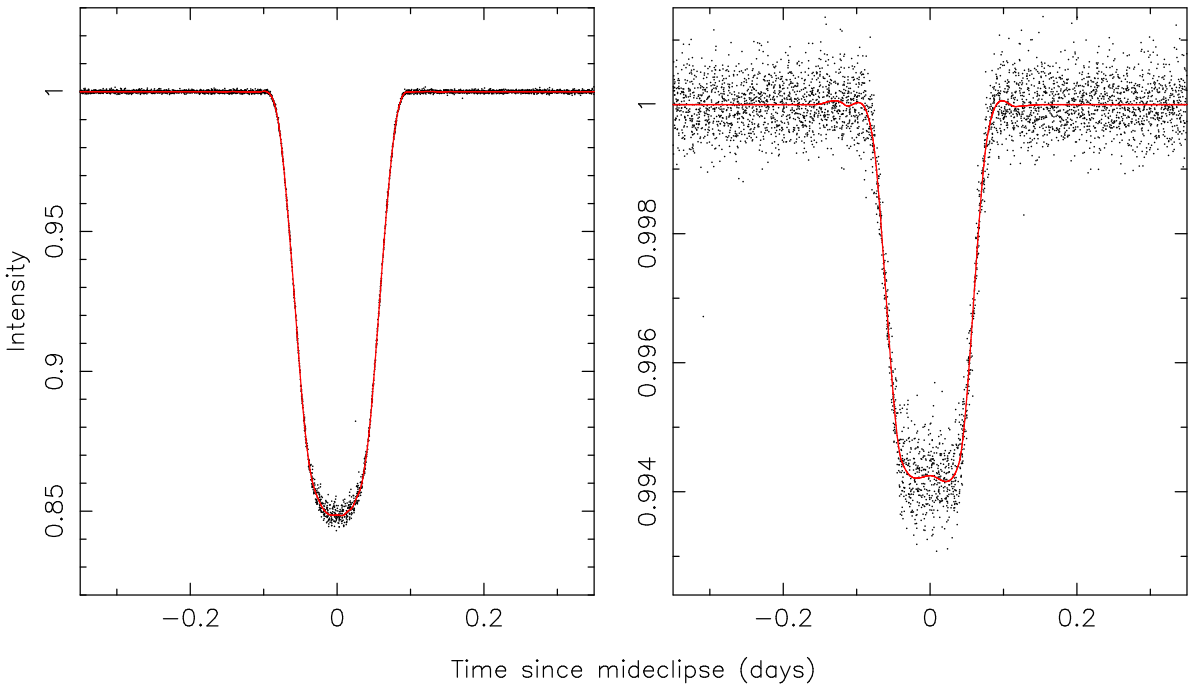

Figure S6: **Mean primary and secondary eclipse profiles.** The observed profiles for the primary eclipse (dots, left panel) and the secondary eclipse (dots, right panel) arrived at after an iterative process. The Piecewise Cubic Hermit Spline (PCHS) models are shown as the solid lines. The increased scatter in the middle of the primary eclipse is most likely due to the effects of star spots.

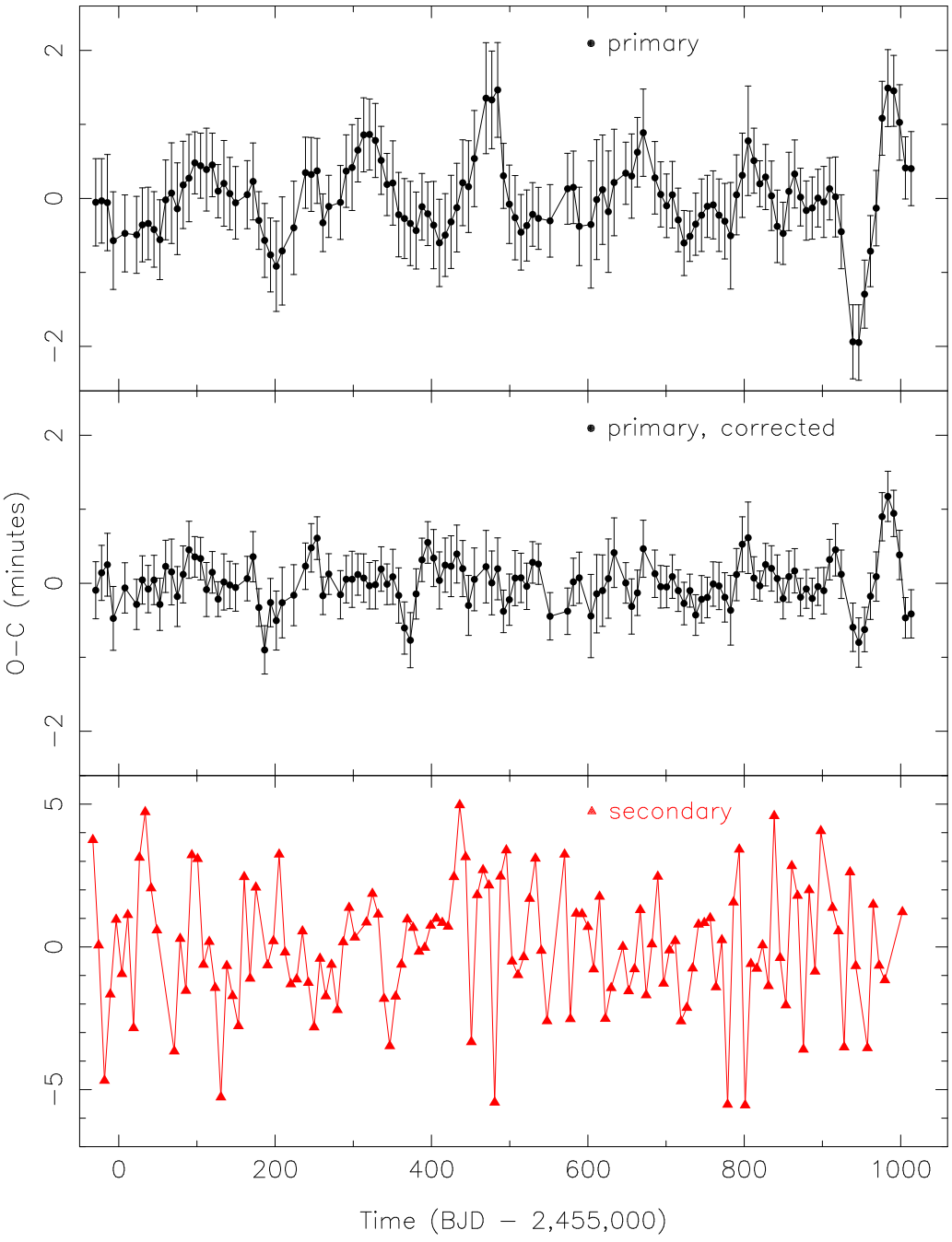

Figure S7: **Observed minus computed curves for the stellar eclipses.** Top: The Observed minus Computed (O-C) residual times of the primary eclipses. Coherent deviations of nearly two minutes are seen, with a quasiperiod of ≈ 178 days. Middle: The O-C times of the primary after correction for the effects of star spots. No periodicities or trends are evident. Bottom: The O-C times for the secondary star. Note the change in the vertical scale. The error bars are not shown for clarity. The scatter is much larger, and no periodicities or trends are seen.

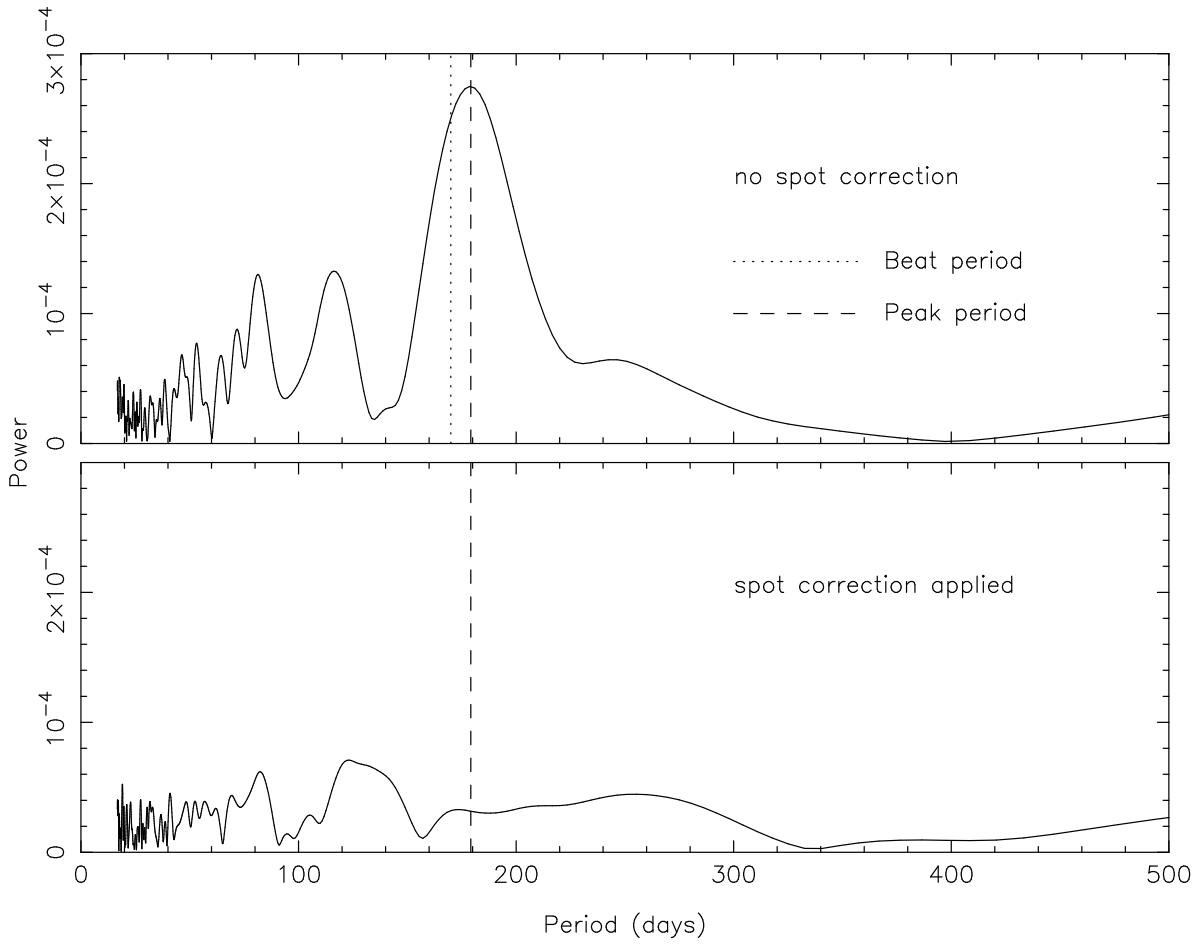

Figure S8: **Lomb-Scargle periodograms of O-C curves.** Top: A Lomb-Scargle periodogram of the O-Cs of the primary eclipses, before any corrections for star spots have been applied. The peak power occurs at a period of 179.2 days (dashed line). The expected beat period of $\approx$ 170 days is indicated by the dotted line. Bottom: A Lomb-Scargle periodogram of the primary eclipse O-Cs after a correction for the effects of star spots has been applied. There is no significant power at any period.

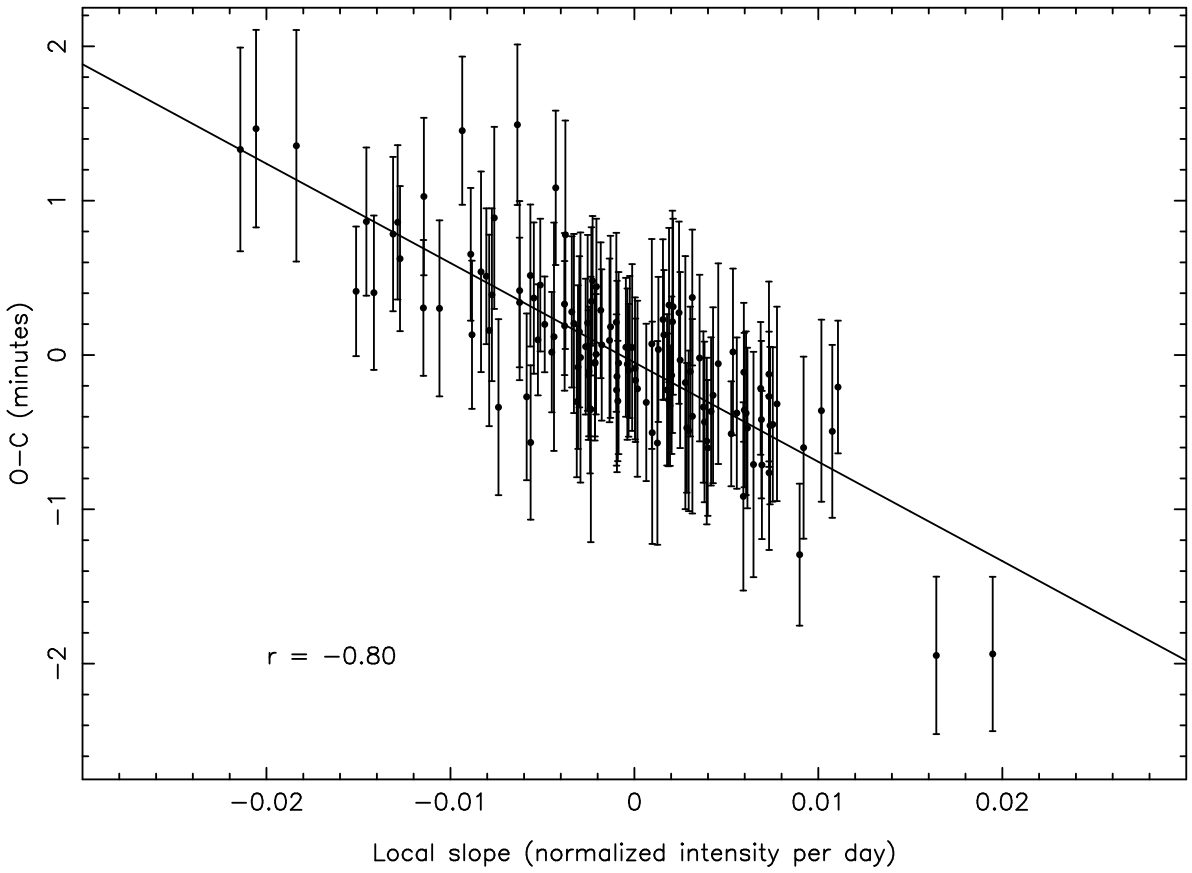

Figure S9: **The correlation of residual O-C time and local slope near primary eclipse.** The dependence of the primary eclipse O-C times on the local SAP light curve slope is shown. A clear correlation is seen. The best-fitting line has a coefficient of correlation of $r = -0.80$.

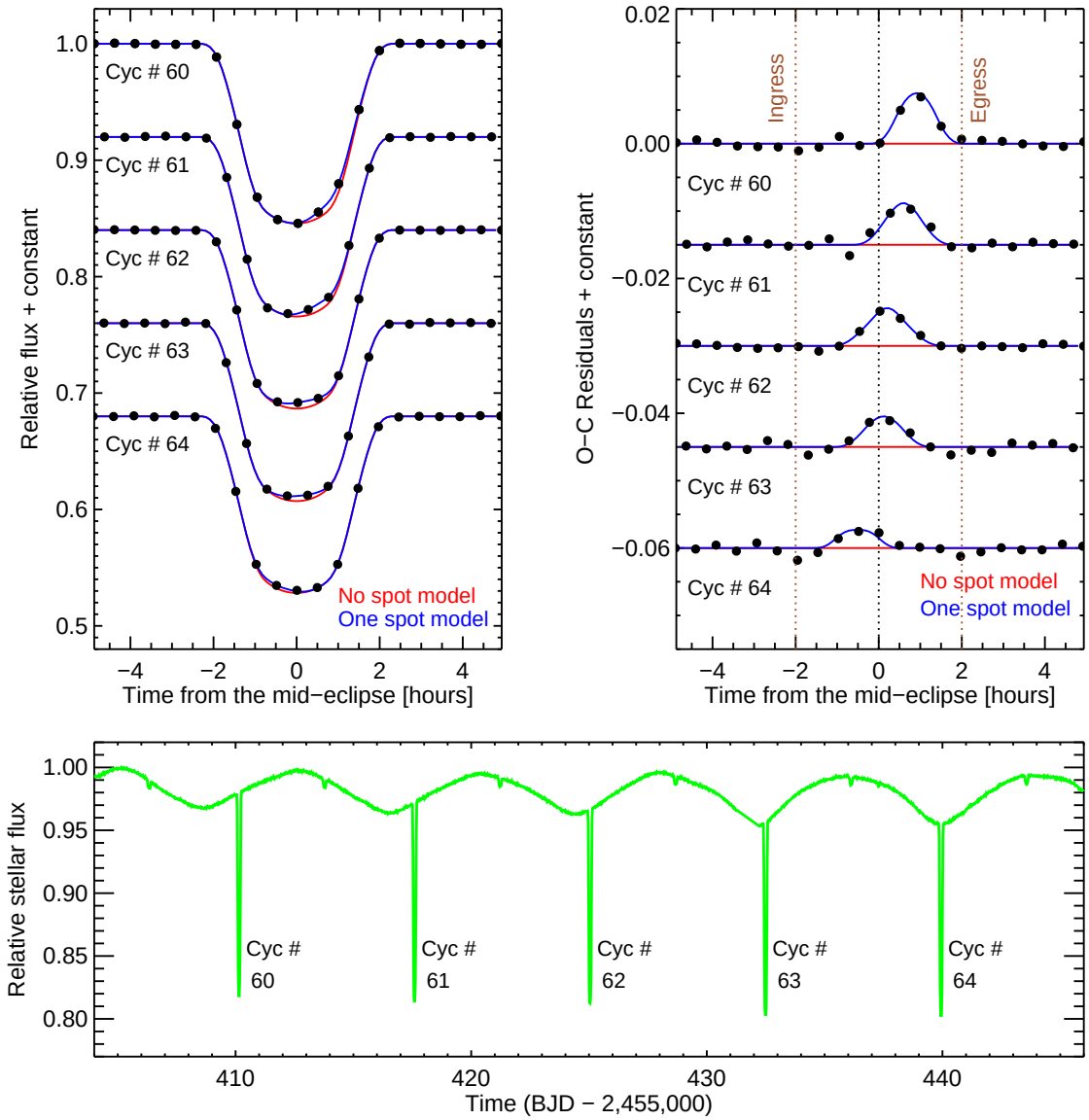

Figure S10: **The effect of star-spots on the primary eclipses.** Upper Left: The observed eclipse light curves (black dots) for five consecutive primary eclipses are shown. A model with no spots (red curves) does not fit the data well, whereas a model with a spot that is occulted by the secondary star fits much better (blue curves). Upper Right: The residuals for the same eclipses are shown. As time passes (top to bottom) the residual feature from the no-spot model moves from the right side of the eclipse to the left. Lower: A section of the light curve spanning eclipse cycles 60–64 is shown. Notice how the local slope in the immediate vicinity of the primary eclipse slowly changes from cycle to cycle.

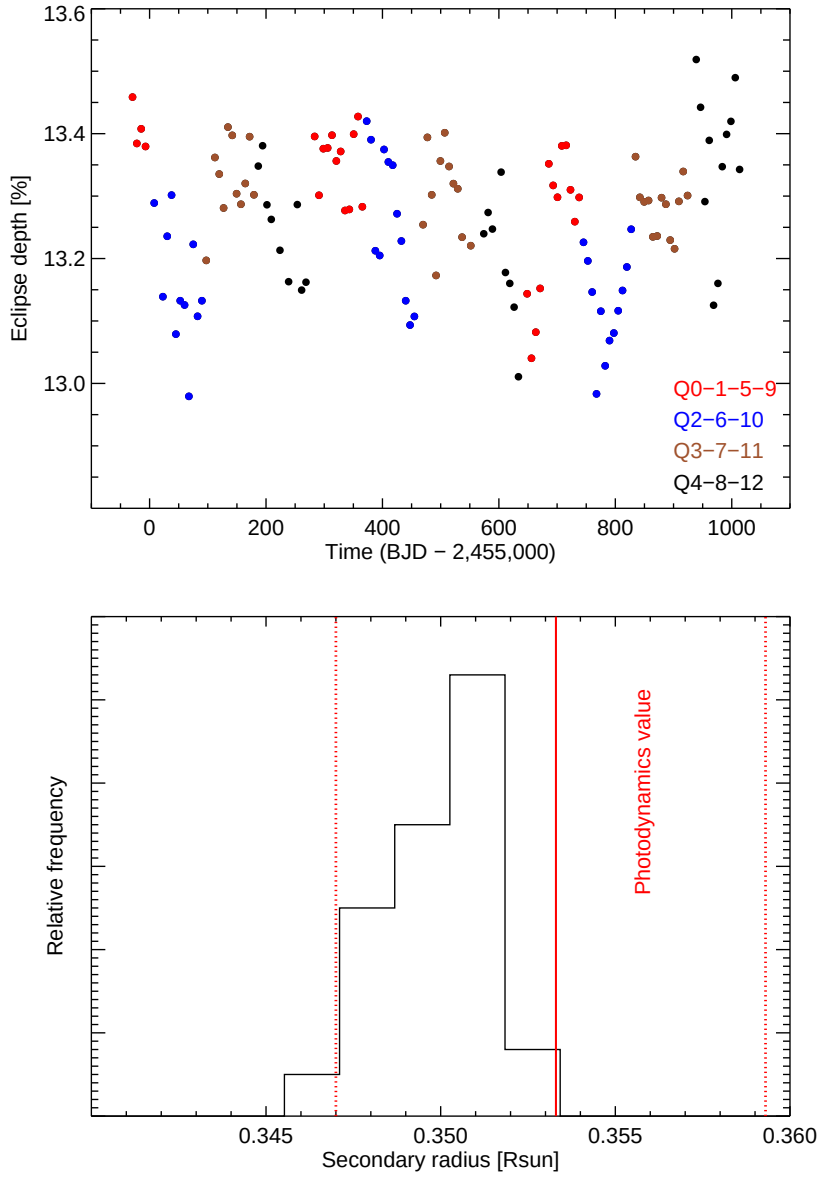

Figure S11: **Eclipse depth variation and its effect on the secondary star radius estimate.** Top: The individual depths for each primary eclipse calculated with a one-spot model are shown (different color correspond to different observing seasons). The depth changes with time because the fraction of the star covered by spots changes with time. There is also a hint that the depths change with the observing season (each season the star falls into a different CCD, changing the level of contamination). Bottom: A histogram of the inferred radius of the secondary star (black line) for each eclipse is shown. This demonstrates how the secondary star radius from the photometric-dynamical model (thick red line) is slightly underestimated (as expected), but the difference is not significant compared to the error bars on the measured radius (the 15.4% and 84.6% confidence levels are shown with dotted red lines).

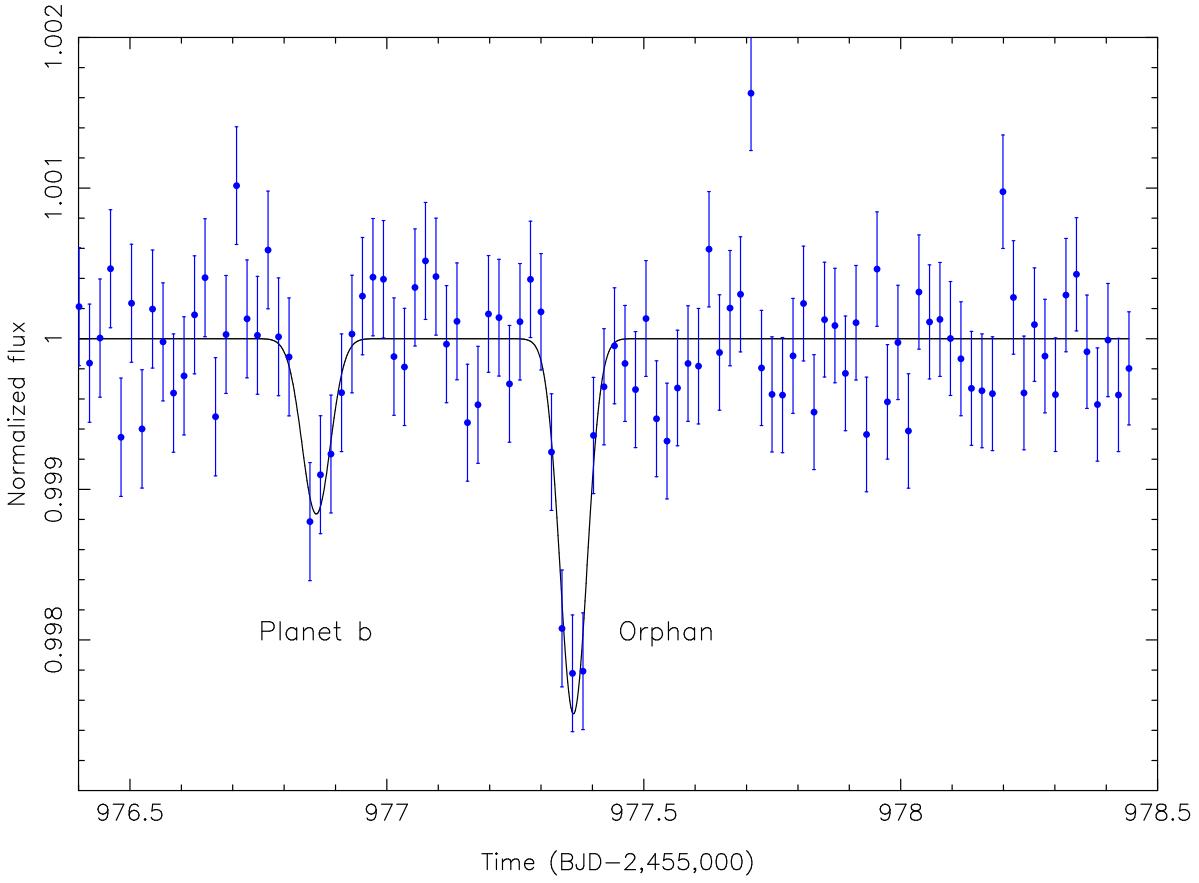

Figure S12: **A segment of the Q12 light curve showing a transit of the inner planet and an orphan transit.** An "orphan" transit that cannot be accounted for by the inner or outer planets appears near the middle of this data segment, about 12 hours after a transit of the inner planet (left). The solid line is a simple model consisting of two Gaussians used to find the mid-transit time of the orphan and to evaluate the significance of the event.

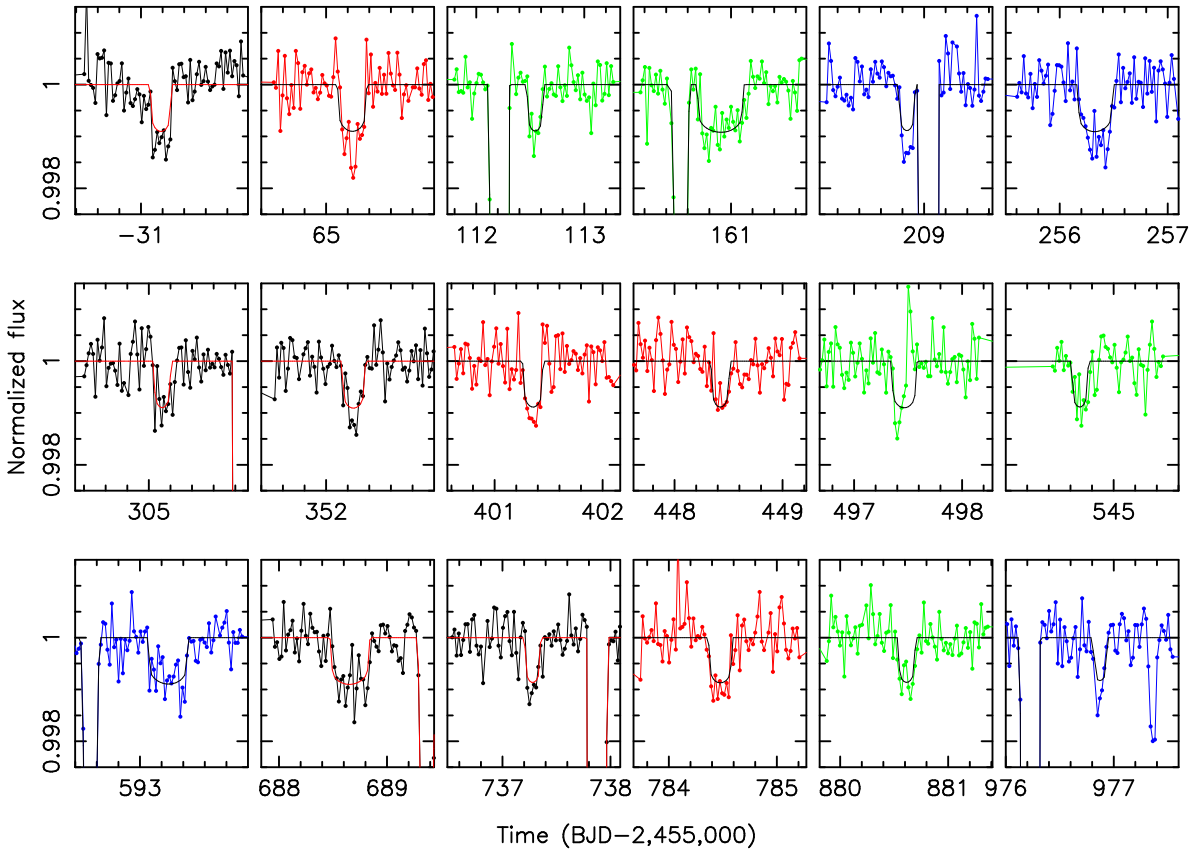

Figure S13: **All observed transits of the inner planet.** The complete set of planet b transits with the best-fitting model is shown. The color coding is the same as in Fig. S1.

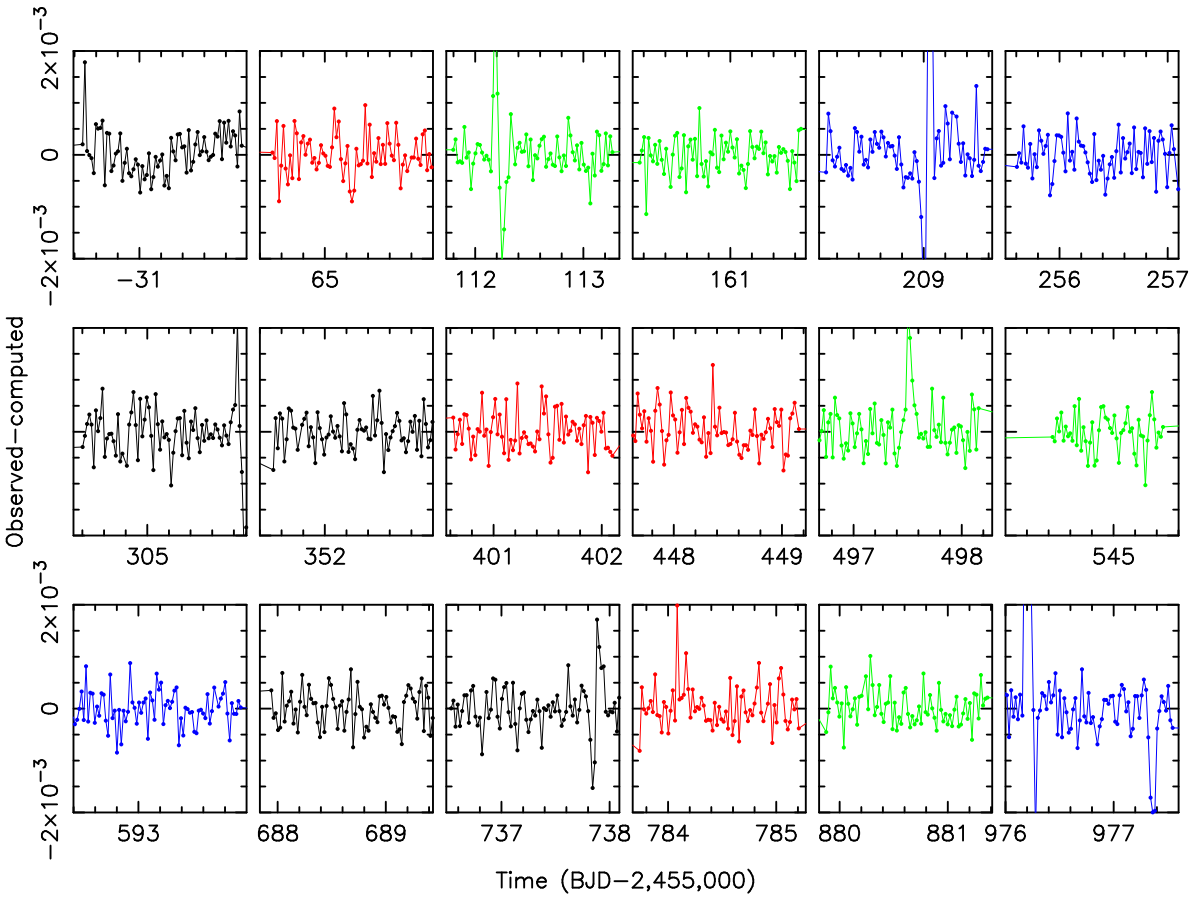

Figure S14: **The residuals of the model fits of the inner planet transits.** The residuals of the model fits of the transits due to the inner planet displayed in Fig. S13 are shown. The color coding is the same as in Fig. S1.

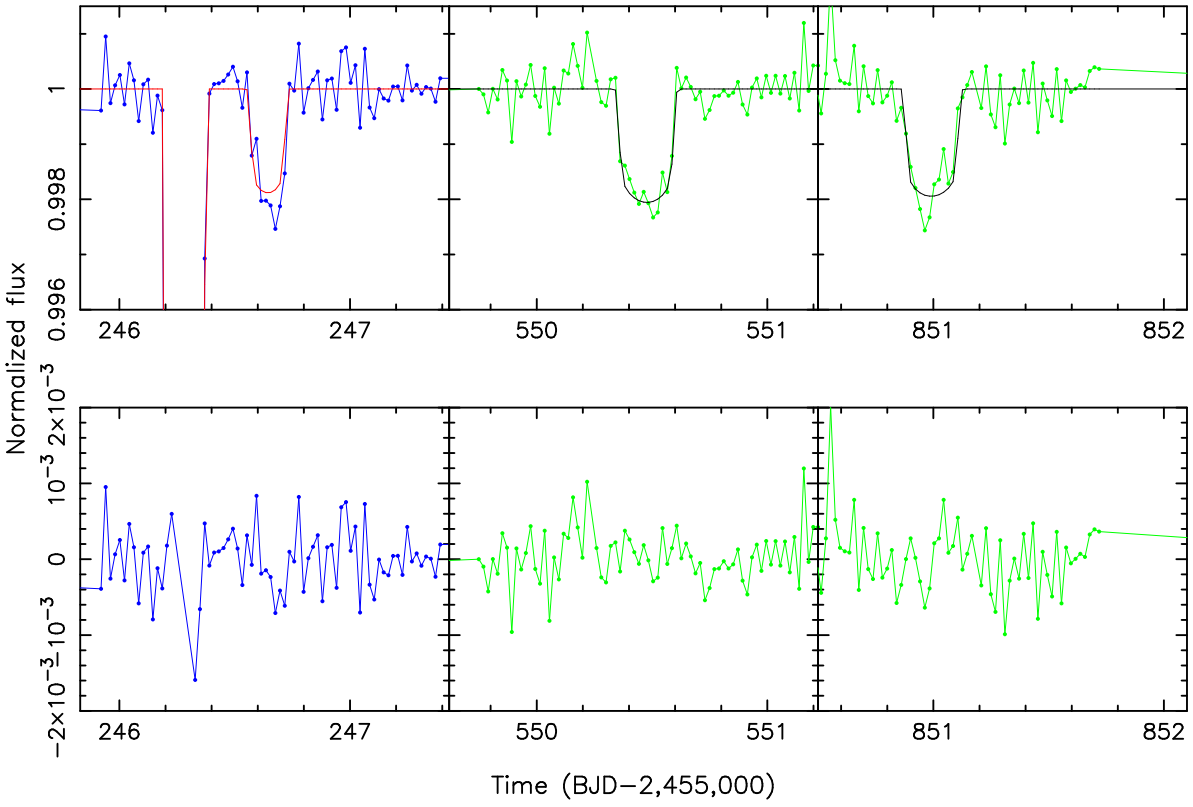

Figure S15: **The model fits and residuals of the transits of the outer planet.** The model fits to the transits of the outer planet are displayed in the top panels, and the residuals are shown in the lower panels. The color coding is the same as in Fig. S1.

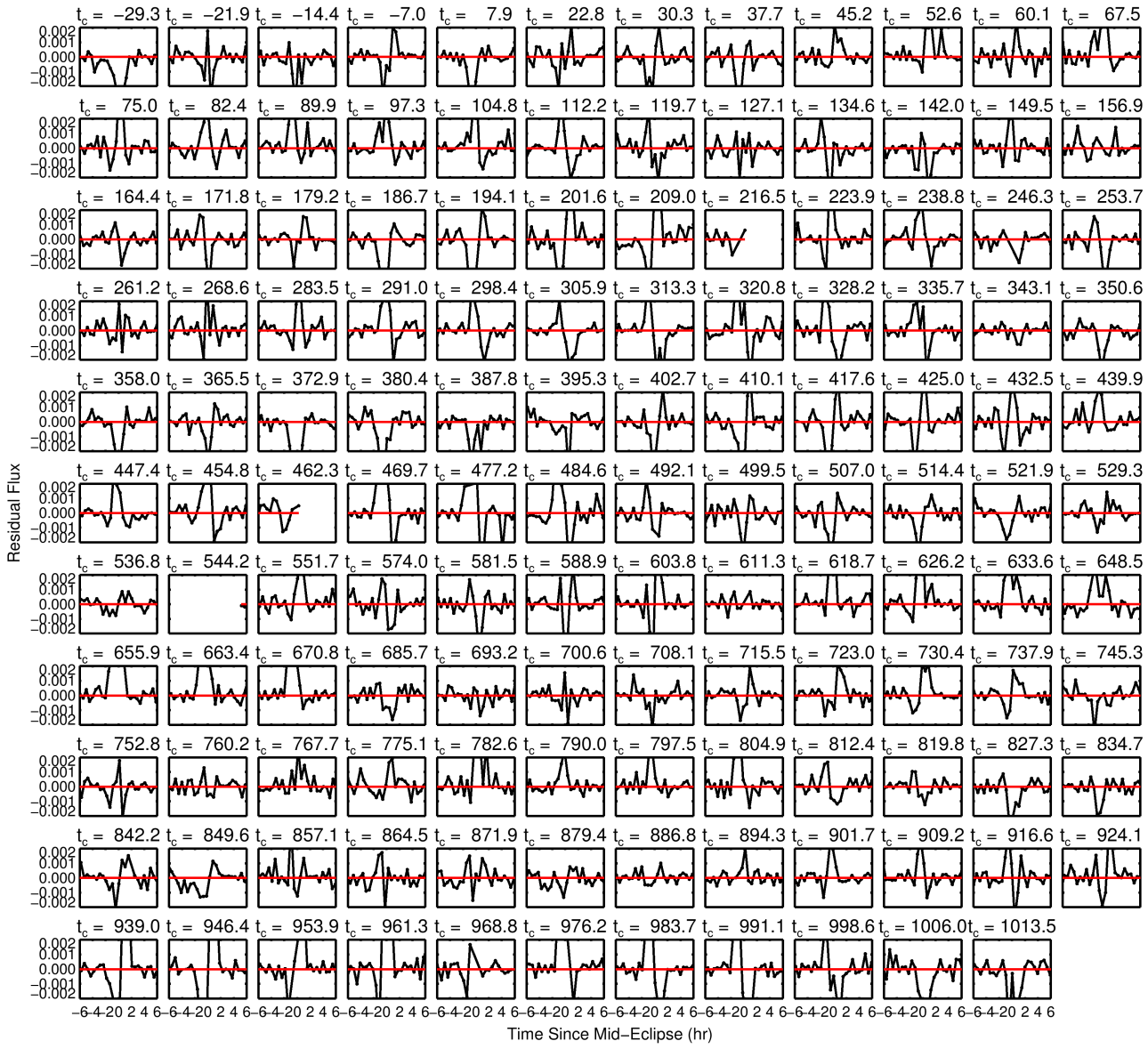

Figure S16: **The residuals of the fits to the primary eclipses.** The residuals during each primary eclipse are displayed. As expected, numerous spot crossing events are seen.

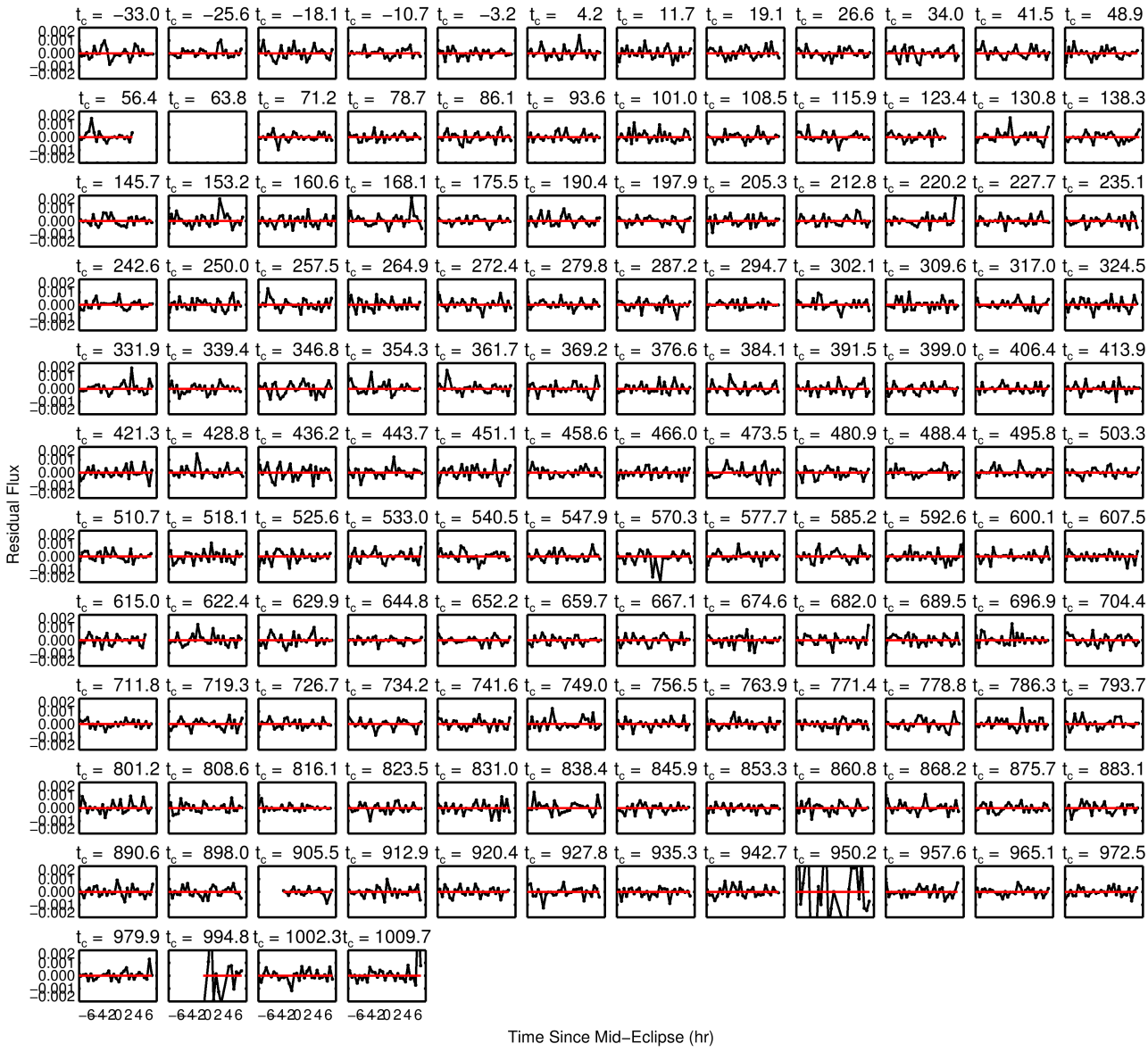

Figure S17: **The residuals of the fits to the secondary eclipses.** The residuals during each secondary eclipse are shown. As these eclipses are total there is much less structure seen in the residuals, compared to the residuals for the primary eclipses displayed in Fig. S16.

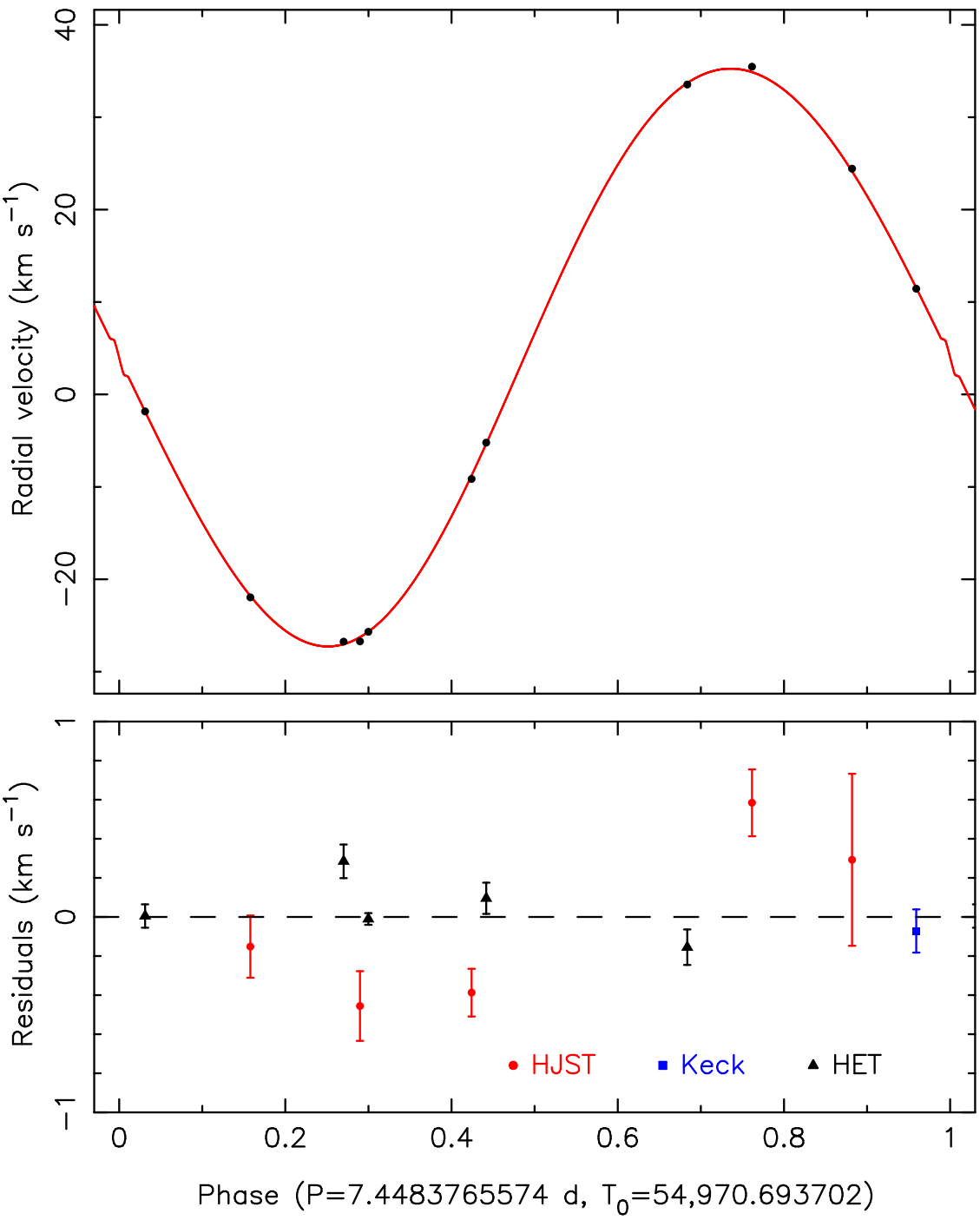

Figure S18: **The observed and model radial velocity curve for the primary.** Top: The radial velocity measurements shown as a function of orbital phase and the best-fitting model. Bottom: The residuals of the fit. Measurements from each telescope+instrument combination are denoted with different symbols and colors.

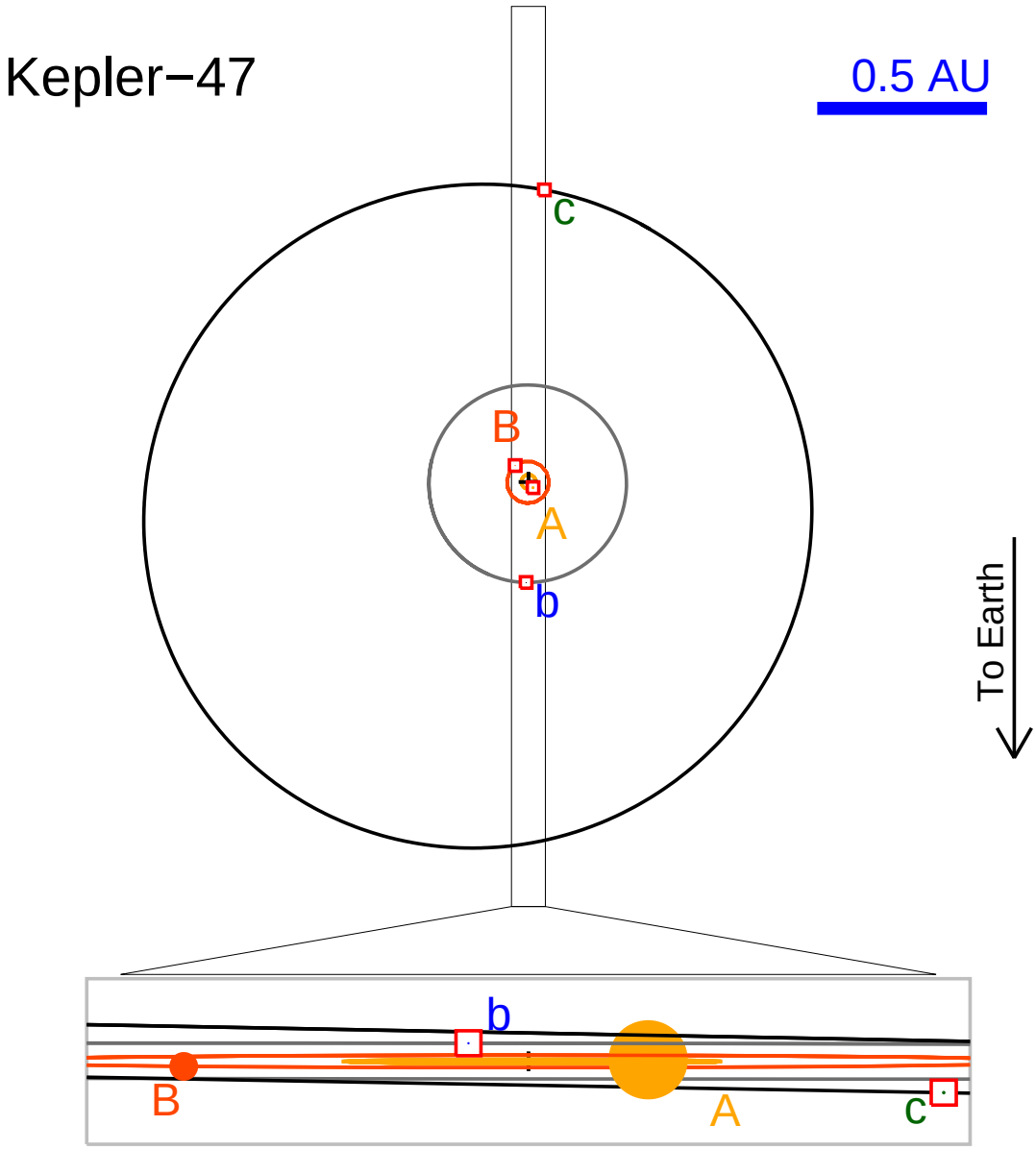

Figure S19: **Schematic diagrams of the Kepler-47 orbits.** Top: A face-on view of the stellar and planetary orbits found from the best-fitting model of the Kepler-47 system. The center of mass of the system is marked with the cross. The stars and the planets would not be seen at this scale, and so their positions are marked with boxes. Bottom: The view of the system as seen from Earth on an expanded scale is shown. The lines denote the projected orbits of the various bodies. Both planets can transit the primary star (labeled A). Transits of the secondary star (labeled b) are narrowly missed for the best-fitting orbital configuration.

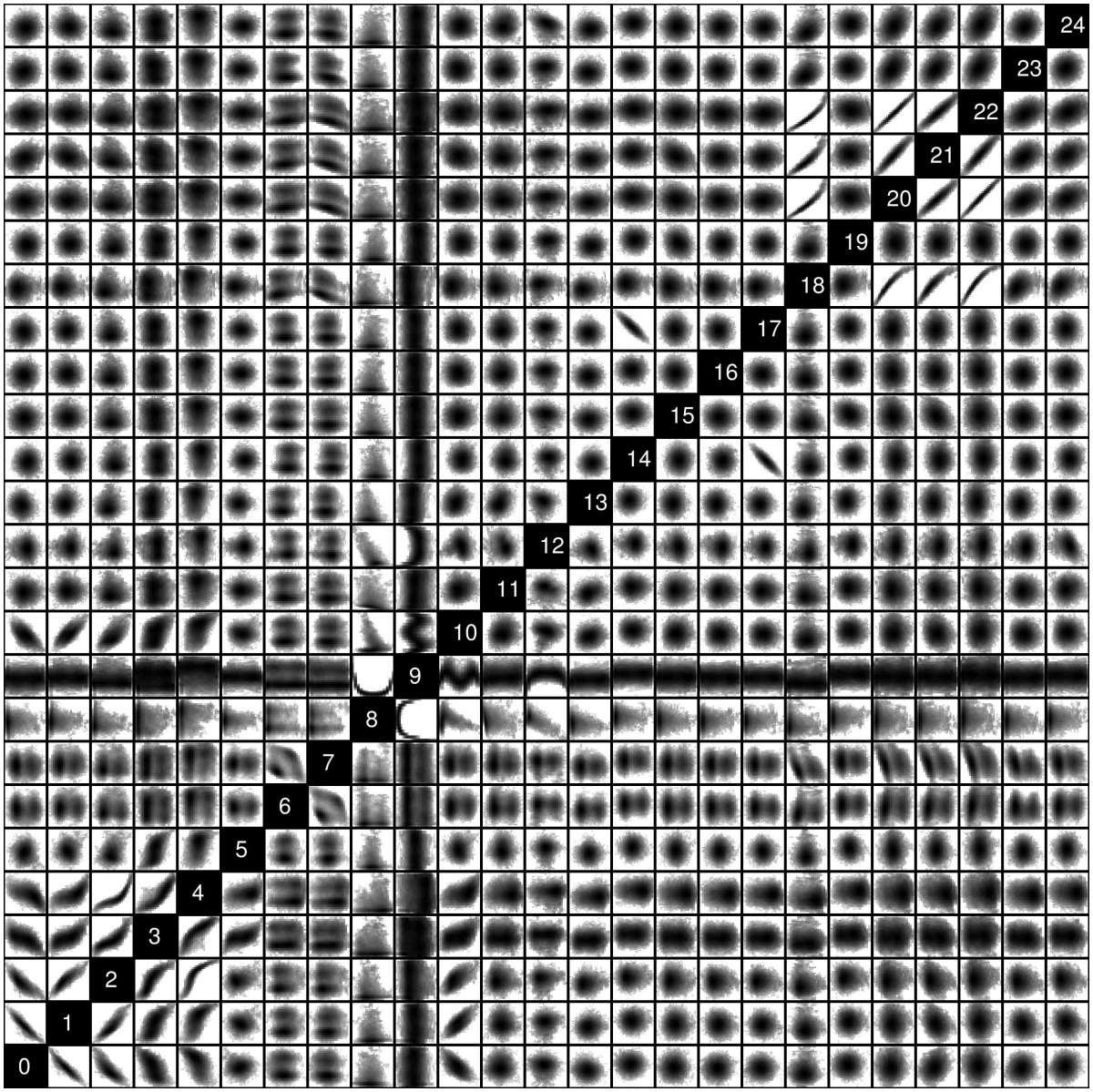

Figure S20: **Two-parameter joint posterior distributions of primary model parameters.** The densities are plotted logarithmically in order to elucidate the nature of the parameter correlations. The indices listed along the diagonal indicate which parameter is associated with the corresponding row and column. The parameter name corresponding to a given index is indicated in Table S5 in the first column.

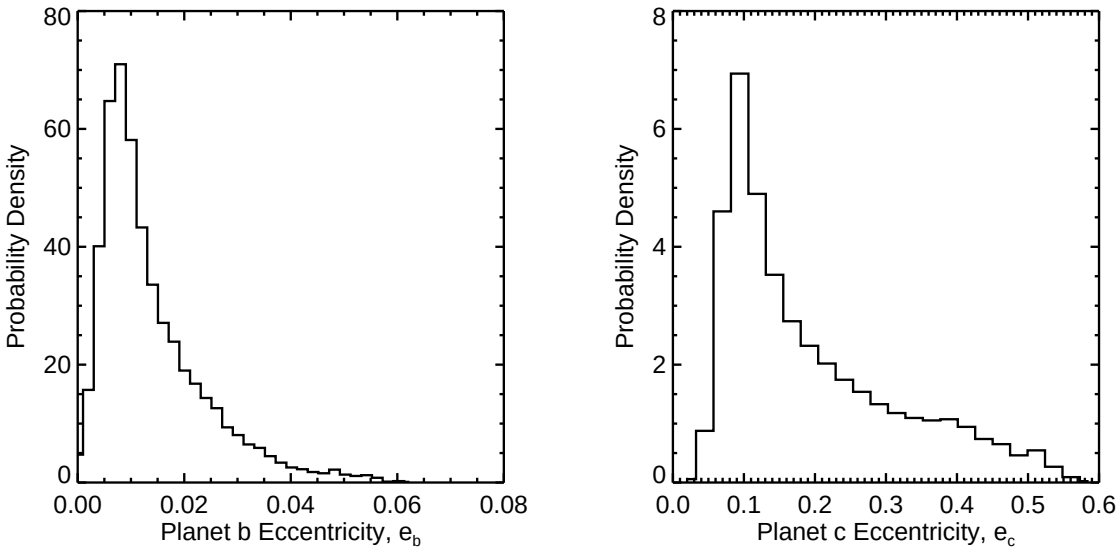

Figure S21: **Posterior distributions in eccentricity.**

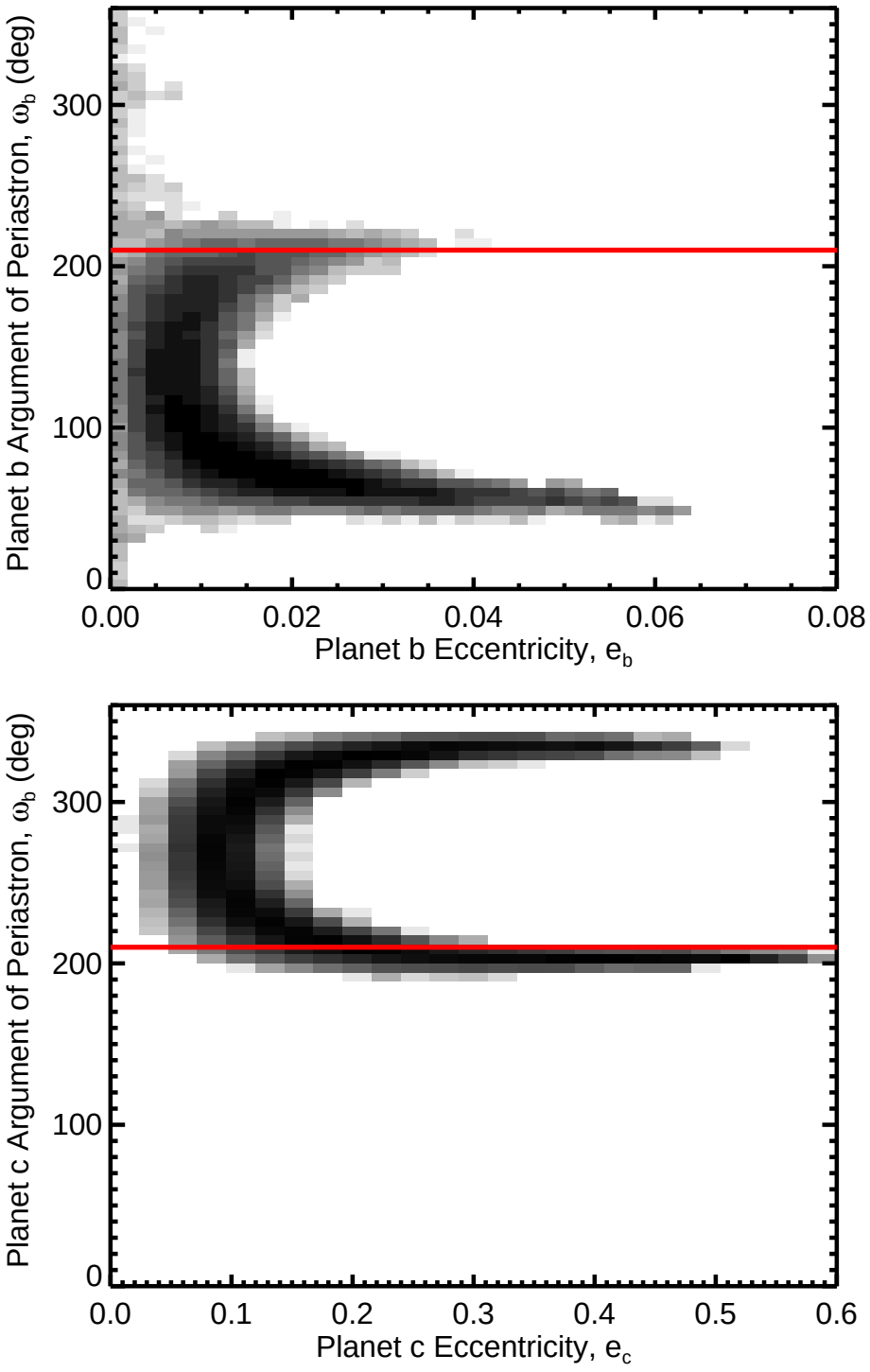

Figure S22: **Posterior distributions in the eccentricity and argument of pericenter planes.**

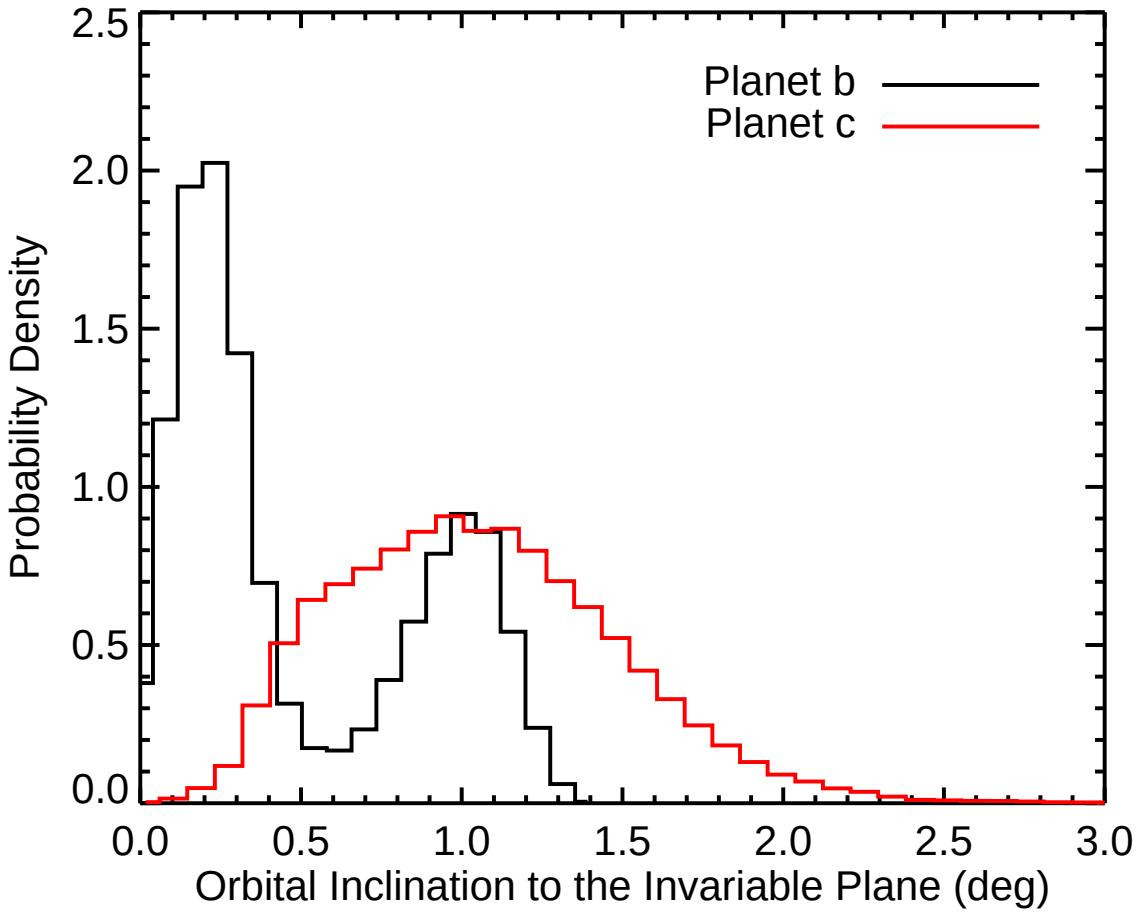

Figure S23: **Posterior distributions in the inclination of the planetary orbits relative to the invariable plane.**

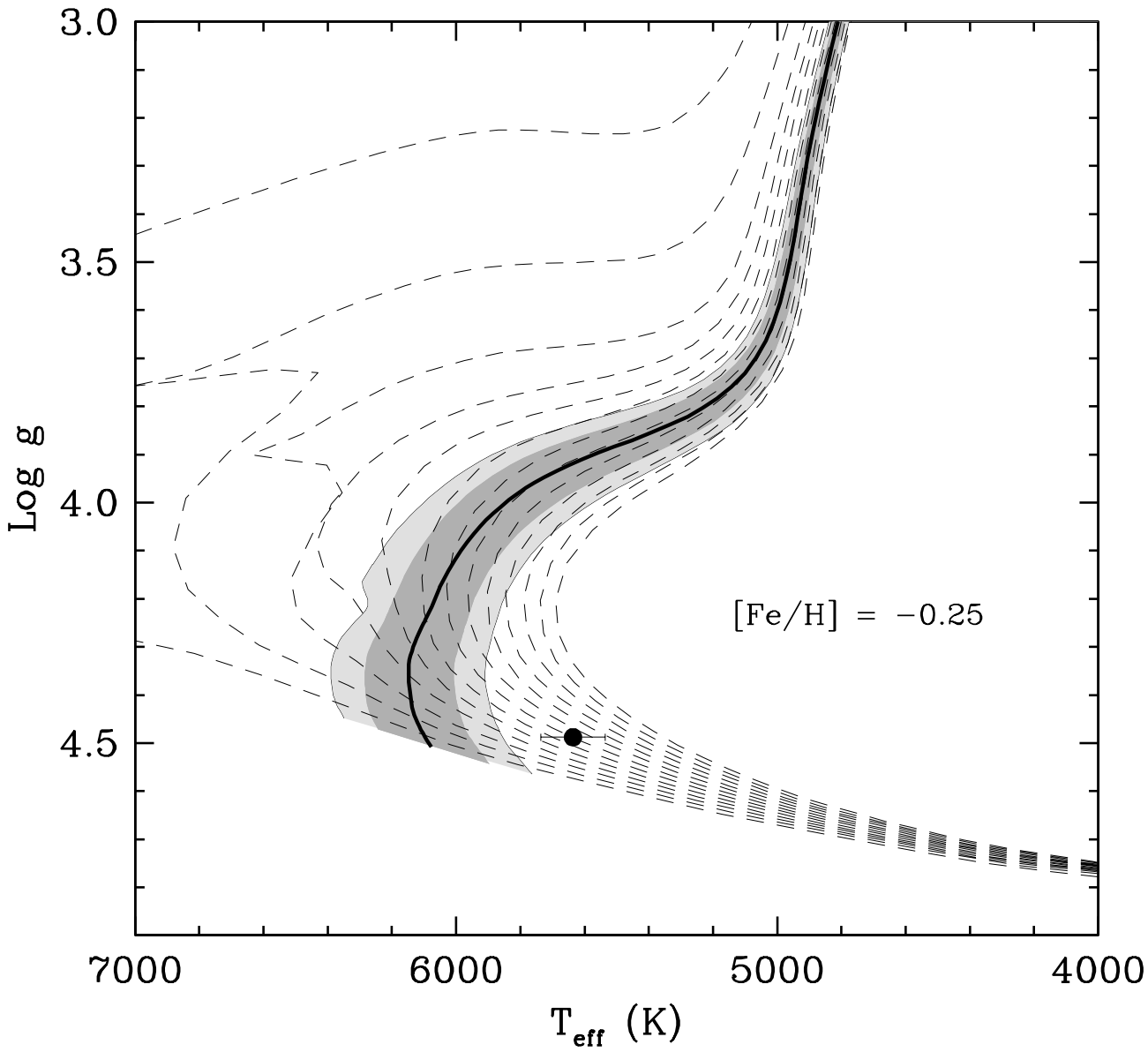

Figure S24: **Comparison of the absolute dimensions of the primary of Kepler-47 against stellar evolution theory.** The thick solid line shows an evolutionary track from the Yonsei-Yale series (*53*,*54*) interpolated to the measured mass of that star and its measured metallicity. The 1σ uncertainty in the location of the track due to the mass error is indicated with the darker shaded area. The wider light shaded area includes the additional 1σ contribution from the uncertainty in [Fe/H]. Isochrones from 1 to 13 Gyr (left to right) are shown with dashed lines.

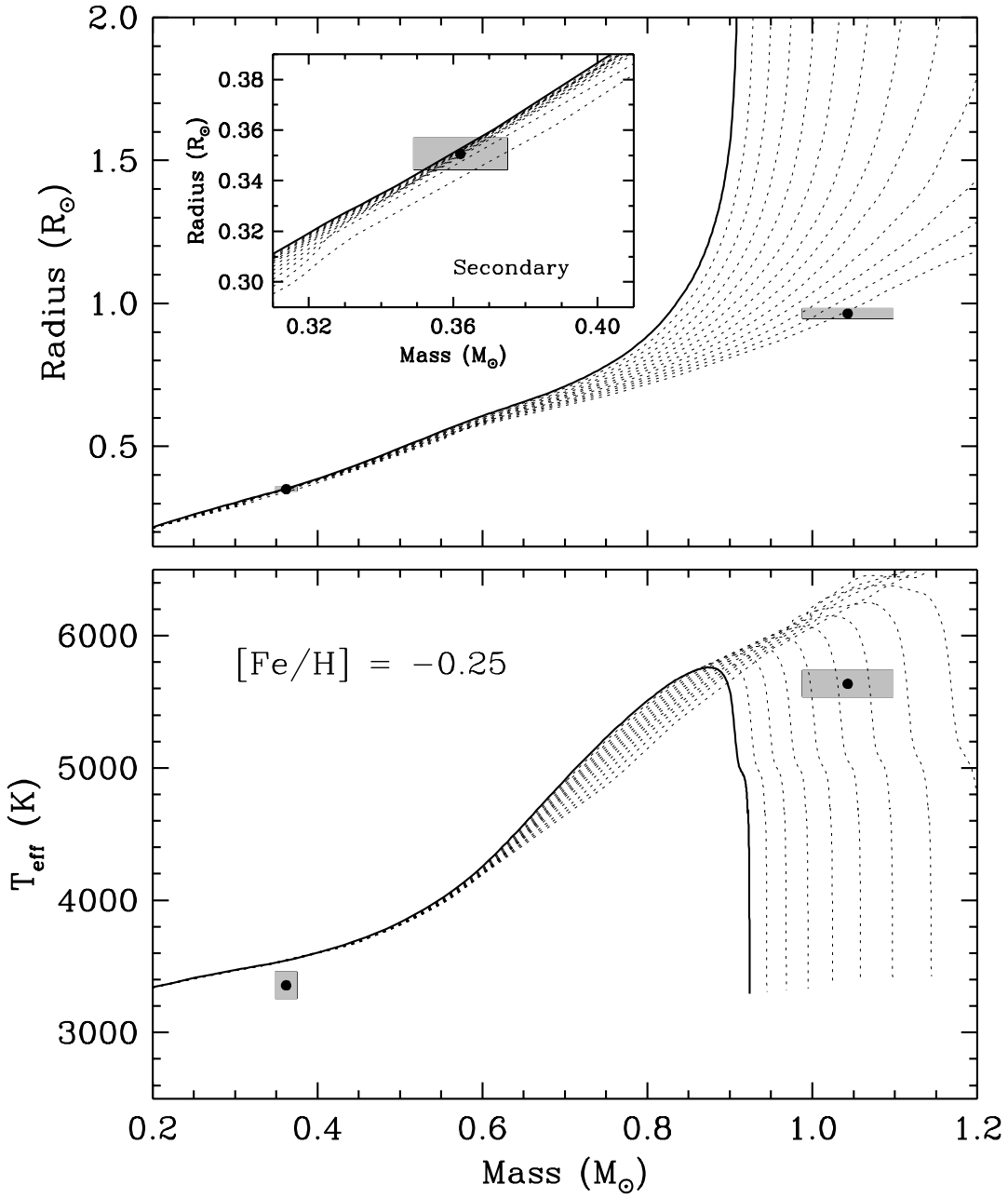

Figure S25: **Isochrones in the mass-radius and mass-temperature planes.** Isochrones from the Dartmouth models (*56*) corresponding to ages from 1 to 13 Gyr, compared against the measured masses, radii, and temperatures of the stars in Kepler-47. The oldest isochrone is indicated with a solid line, and the metallicity has been set to the spectroscopically determined value of [Fe/H]$= -0.25$. The error bars for the measurements are represented with the shaded boxes. Top: The mass-radius diagram. The inset shows an enlargement around the secondary, which appears to agree with the models. Bottom: The mass-temperature diagram, showing the secondary to be cooler than predicted.

Table S1: **Radial velocities for Kepler-47.**

Date YYYY-MM-DD	UT Time	BJD (2,455,000+)	RV_A km s^{-1}	telescope
2012-04-10	13:25:48.68	1028.05942	11.442 ± 0.011	Keck
2012-04-23	09:11:27.36	1040.90325	33.534 ± 0.091	HET
2012-05-01	09:52:55.08	1048.93237	35.458 ± 0.171	HJST
2012-05-02	07:23:45.95	1049.82882	24.430 ± 0.440	HJST
2012-05-04	08:34:10.40	1051.88474	-21.957 ± 0.159	HJST
2012-05-05	08:08:26.83	1052.86692	-26.719 ± 0.178	HJST
2012-05-06	08:08:55.42	1053.86729	-9.150 ± 0.122	HJST
2012-05-18	07:35:21.15	1065.83749	-1.843 ± 0.060	HET
2012-05-20	07:37:07.78	1067.83880	-25.681 ± 0.030	HET
2012-06-05	06:29:24.15	1083.79236	-5.223 ± 0.080	HET
2012-06-26	08:03:52.39	1104.85862	-26.743 ± 0.086	HJST

Table S2: **Spectroscopic parameters from SPC.**

parameter	value
$T_{\rm eff}$ (K)	5636 ± 100
$\log g$ (cgs dex)	4.42 ± 0.10
[m/H] (dex)	-0.25 ± 0.08
$V_{\rm rot} \sin i$ (km s^{-1})	4.1 ± 0.5

Table S3: **Times of stellar eclipses.**

cycle #	primary time[2]	corrected time[1]	uncertainty (min)	cycle #	secondary time[1]	uncertainty (min)
0.0	...	...	...	0.4873910	-33.12216	2.18
1.0	-29.30630	-29.30631	0.39	1.4873910	-25.67634	2.58
2.0	-21.85791	-21.85777	0.37	2.4873910	-18.23125	2.18
3.0	-14.40955	-14.40931	0.42	3.4873910	-10.78077	2.18
4.0	-6.96153	-6.96144	0.43	4.4873910	-3.33057	2.18
5.0	...	...	...	5.4873910	4.11649	2.18
6.0	7.93529	7.93560	0.34	6.4873910	11.56631	2.48
7.0	...	...	...	7.4873910	19.01194	2.28
8.0	22.83203	22.83220	0.34	8.4873910	26.46447	2.38

[2]BJD-2,455,000

Table S3: (continued)

9.0	30.28050	30.28080	0.33	9.4873910	33.91396	2.08
10.0	37.72889	37.72909	0.32	10.4873910	41.36049	2.28
11.0	45.17721	45.17755	0.33	11.4873910	48.80785	2.18
12.0	52.62549	52.62570	0.35	12.4873910	...	...
13.0	60.07424	60.07443	0.35	13.4873910	...	...
14.0	67.52268	67.52276	0.44	14.4873910	71.15005	2.18
15.0	74.97091	74.97090	0.41	15.4873910	78.60117	2.38
16.0	82.41951	82.41949	0.39	16.4873910	86.04829	2.18
17.0	89.86795	89.86809	0.39	17.4873910	93.49997	2.18
18.0	97.31647	97.31640	0.27	18.4873910	100.94826	2.38
19.0	104.76482	104.76476	0.29	19.4873910	108.39407	2.18
20.0	112.21316	112.21285	0.37	20.4873910	115.84301	2.18
21.0	119.66158	119.66138	0.28	21.4873910	123.29027	2.28
22.0	127.10971	127.10951	0.24	22.4873910	130.73599	2.18
23.0	134.55816	134.55805	0.38	23.4873910	138.18757	2.28
24.0	142.00644	142.00639	0.32	24.4873910	145.63522	2.38
25.0	149.45473	149.45475	0.32	25.4873910	153.08287	2.28
26.0	...	...	...	26.4873910	160.53488	2.48
27.0	164.35156	164.35158	0.30	27.4873910	167.98079	2.08
28.0	171.80006	171.80016	0.34	28.4873910	175.43139	2.18
29.0	179.24807	179.24806	0.25	29.4873910	...	...
30.0	186.69626	186.69604	0.33	30.4873910	190.32626	2.18
31.0	194.14450	194.14486	0.33	31.4873910	197.77523	2.28
32.0	201.59277	201.59307	0.40	32.4873910	205.22572	2.18
33.0	209.04129	209.04161	0.48	33.4873910	212.67172	2.18
34.0	...	...	...	34.4873910	220.11933	2.18
35.0	223.93826	223.93843	0.41	35.4873910	227.56783	2.28
36.0	...	...	...	36.4873910	235.01738	2.18
37.0	238.83553	238.83546	0.31	37.4873910	242.46451	2.18
38.0	246.28389	246.28401	0.33	38.4873910	249.91181	2.18
39.0	253.73230	253.73247	0.29	39.4873910	257.36186	2.58
40.0	261.18019	261.18031	0.25	40.4873910	264.80933	2.18
41.0	268.62872	268.62889	0.27	41.4873910	272.25848	2.18
42.0	...	...	...	42.4873910	279.70576	2.18
43.0	283.52551	283.52545	0.33	43.4873910	287.15579	2.58
44.0	290.97418	290.97397	0.32	44.4873910	294.60501	2.18
45.0	298.42259	298.42234	0.38	45.4873910	302.05267	2.18
46.0	305.87113	305.87077	0.28	46.4873910	...	...
47.0	313.31965	313.31911	0.33	47.4873910	316.94980	2.18

Table S3: (continued)

48.0	320.76803	320.76741	0.31	48.4873910	324.39888	2.18
49.0	328.21635	328.21580	0.33	49.4873910	331.84676	2.08
50.0	335.66454	335.66432	0.30	50.4873910	339.29309	2.28
51.0	343.11269	343.11255	0.27	51.4873910	346.74032	2.18
52.0	350.56108	350.56100	0.37	52.4873910	354.18991	2.28
53.0	358.00916	358.00920	0.37	53.4873910	361.63907	2.18
54.0	365.45750	365.45727	0.35	54.4873910	369.08855	2.18
55.0	372.90583	372.90553	0.37	55.4873910	376.53673	2.38
56.0	380.35414	380.35434	0.34	56.4873910	383.98453	2.38
57.0	387.80274	387.80304	0.29	57.4873910	391.43301	2.38
58.0	395.25105	395.25158	0.28	58.4873910	398.88193	2.28
59.0	402.69932	402.69981	0.39	59.4873910	406.33048	2.28
60.0	410.14753	410.14797	0.39	60.4873910	413.77876	2.48
61.0	417.59598	417.59649	0.37	61.4873910	421.22705	2.28
62.0	425.04448	425.04486	0.41	62.4873910	428.67664	2.18
63.0	432.49299	432.49335	0.39	63.4873910	436.12677	2.48
64.0	439.94160	439.94159	0.38	64.4873910	443.57389	2.28
65.0	447.38994	447.38962	0.41	65.4873910	451.01777	2.28
66.0	454.83858	454.83824	0.42	66.4873910	458.46973	2.28
67.0	...	...	...	67.4873910	465.91872	2.18
68.0	469.73590	469.73511	0.49	68.4873910	473.36673	2.18
69.0	477.18426	477.18334	0.43	69.4873910	480.80983	2.18
70.0	484.63273	484.63184	0.42	70.4873910	488.26371	2.18
71.0	492.08030	492.07982	0.29	71.4873910	495.71273	2.08
72.0	499.52841	499.52831	0.35	72.4873910	503.15841	2.28
73.0	506.97666	506.97688	0.37	73.4873910	510.60646	2.28
74.0	514.42490	514.42526	0.33	74.4873910	518.05528	2.18
75.0	521.87334	521.87356	0.31	75.4873910	525.50508	2.28
76.0	529.32182	529.32216	0.28	76.4873910	532.95444	2.38
77.0	536.77016	536.77052	0.27	77.4873910	540.40058	2.28
78.0	...	...	...	78.4873910	547.84725	2.38
79.0	551.66689	551.66678	0.32	79.4873910	...	...
80.0	...	...	...	80.4873910	...	...
81.0	...	...	...	81.4873910	570.19645	2.88
82.0	574.01232	574.01196	0.31	82.4873910	577.64083	2.38
83.0	581.46071	581.46061	0.32	83.4873910	585.09178	2.38
84.0	588.90872	588.90902	0.35	84.4873910	592.54015	2.18
85.0	...	...	...	85.4873910	599.98822	2.08
86.0	603.80549	603.80542	0.56	86.4873910	607.43557	2.28

Table S3: (continued)

87.0	611.25410	611.25400	0.53	87.4873910	614.88572	2.08
88.0	618.70257	618.70241	0.48	88.4873910	622.33113	2.38
89.0	626.15074	626.15090	0.54	89.4873910	629.78026	2.18
90.0	633.59939	633.59952	0.47	90.4873910	...	...
91.0	...	...	...	91.4873910	644.67803	2.18
92.0	648.49623	648.49598	0.27	92.4873910	652.12533	2.18
93.0	655.94458	655.94414	0.37	93.4873910	659.57425	2.18
94.0	663.39318	663.39264	0.31	94.4873910	667.02407	1.98
95.0	670.84174	670.84143	0.39	95.4873910	674.47038	2.18
96.0	...	...	...	96.4873910	681.92000	2.28
97.0	685.73807	685.73795	0.32	97.4873910	689.37003	2.28
98.0	693.18629	693.18620	0.29	98.4873910	696.81581	2.08
99.0	700.63456	700.63458	0.28	99.4873910	704.26500	2.08
100.0	708.08304	708.08305	0.29	100.4873910	711.71361	2.08
101.0	715.53118	715.53130	0.28	101.4873910	719.16004	2.18
102.0	722.97934	722.97955	0.29	102.4873910	726.60875	2.18
103.0	730.42778	730.42805	0.22	103.4873910	734.05809	2.18
104.0	737.87627	737.87620	0.27	104.4873910	741.50754	2.18
105.0	745.32473	745.32472	0.32	105.4873910	748.95596	2.18
106.0	752.77319	752.77311	0.27	106.4873910	756.40446	2.28
107.0	760.22158	760.22162	0.30	107.4873910	763.85116	2.28
108.0	767.66986	767.66997	0.32	108.4873910	771.30069	2.28
109.0	775.11818	775.11824	0.33	109.4873910	778.74507	2.28
110.0	782.56642	782.56650	0.47	110.4873910	786.19837	2.48
111.0	790.01518	790.01521	0.35	111.4873910	793.64804	2.08
112.0	797.46374	797.46387	0.37	112.4873910	801.09020	2.28
113.0	804.91244	804.91231	0.48	113.4873910	808.54202	2.18
114.0	812.36063	812.36030	0.29	114.4873910	815.99029	2.38
115.0	819.80879	819.80861	0.20	115.4873910	823.43924	2.18
116.0	827.25723	827.25718	0.29	116.4873910	830.88663	2.28
117.0	834.70543	834.70552	0.31	117.4873910	838.33915	2.18
118.0	842.15352	842.15380	0.32	118.4873910	845.78408	2.18
119.0	849.60183	849.60199	0.27	119.4873910	853.23131	2.08
120.0	857.05060	857.05057	0.35	120.4873910	860.68308	2.18
121.0	864.49914	864.49900	0.30	121.4873910	868.13074	2.08
122.0	871.94730	871.94713	0.25	122.4873910	875.57538	2.18
123.0	879.39555	879.39559	0.26	123.4873910	883.02764	2.18
124.0	886.84395	886.84387	0.27	124.4873910	890.47404	2.08
125.0	894.29242	894.29236	0.25	125.4873910	897.92584	2.08

Table S3: (continued)

126.0	901.74076	901.74070	0.31	126.4873910	...	...
127.0	909.18926	909.18937	0.27	127.4873910	912.82074	2.28
128.0	916.63756	916.63783	0.35	128.4873910	920.26855	2.18
129.0	924.08561	924.08598	0.33	129.4873910	927.71411	2.18
130.0	...	...	...	130.4873910	935.16675	2.18
131.0	938.98133	938.98223	0.33	131.4873910	942.61285	2.18
132.0	946.42970	946.43047	0.33	132.4873910	...	...
133.0	953.87853	953.87896	0.30	133.4873910	957.50762	2.28
134.0	961.32731	961.32765	0.31	134.4873910	964.95949	2.68
135.0	968.77609	968.77621	0.33	135.4873910	972.40639	2.18
136.0	976.22531	976.22515	0.33	136.4873910	979.85442	2.28
137.0	983.67397	983.67372	0.34	137.4873910	...	...
138.0	991.12232	991.12194	0.31	138.4873910	...	...
139.0	998.57040	998.56992	0.33	139.4873910	1002.20122	1.98
140.0	1006.01835	1006.01771	0.27	140.4873910	...	...
141.0	1013.46672	1013.46612	0.33	141.4873910	...	...

Table S4: **Times of planetary transits.**

cycle #	measured time[3]	uncertainty (minute)	duration (hour)	model time[2]	model duration (hour)	note
			Planet b			
1.0	-30.79061	11.98	4.80	-30.81466	4.50	
2.0	...	...	...	16.27142	3.81	data gap
3.0	65.24000	30.00	6.72	65.24426	6.23	
4.0	112.53000	30.00	3.60	112.54562	3.53	
5.0	160.94000	90.00	11.00	160.90698	10.29	
6.0	208.84245	5.30	3.60	208.84102	3.50	
7.0	256.35001	60.00	8.16	256.32285	7.80	
8.0	305.13831	0.70	3.84	305.12396	3.71	
9.0	352.26001	30.00	5.28	352.25223	5.00	
10.0	401.35165	8.06	4.56	401.35574	4.24	
11.0	448.43933	19.12	4.08	448.42355	3.94	
12.0	497.42072	60.00	5.76	497.46506	5.50	
13.0	544.74023	10.37	3.60	544.68713	3.48	
14.0	593.25055	2.30	9.12	593.26556	8.77	
15.0	...	...	...	640.98407	3.29	data gap
16.0	688.61578	26.96	9.36	688.65100	8.65	
17.0	737.27374	10.37	3.60	737.27942	3.31	
18.0	784.40002	30.00	5.52	784.47644	5.13	
19.0	...	...	...	833.53937	3.58	data gap
20.0	880.63666	12.21	3.84	880.61505	3.73	
21.0	...	...	...	929.71033	4.30	corrupted data
22.0	976.86499	60.00	4.08	976.87207	3.06	
			Planet c			
1.0	246.64867	5.07	5.76	246.64379	4.02	
2.0	550.47591	5.23	8.16	550.47833	6.12	
3.0	850.99483	5.30	6.96	850.99053	6.00	
			Orphan			
1.0	977.363	5.76	4.15	...	...	

[3]BJD-2,455,000

Table S5: **Model fitting parameters for the photometric-dynamical model.** See the text for definitions of the terms. The numbers in boldface refer to the parameters shown in Fig. S20.

Parameter Name	Best-fit	50%	15.8%	84.2%
Mass parameters				
0. Mass of Star A, M_A ($M_\odot$)	1.043	1.049	-0.055	$+0.054$
1. Mass ratio, Star B, M_B/M_A	0.3473	0.3462	-0.0063	$+0.0069$
Planet b Orbit (Epoch BJD 2,454,969.216)				
2. Orbital Period, P_b (day)	49.514	49.532	-0.027	$+0.040$
3. Eccentricity Parameter, $\sqrt{e_b}\cos(\omega_b)$	-0.094	0.000	-0.075	$+0.067$
4. Eccentricity Parameter, $\sqrt{e_b}\sin(\omega_b)$	0.003	0.098	-0.067	$+0.042$
5. Time of Barycentric Transit, t_b (BJD - 2,455,000)	-31.367	-31.353	-0.010	$+0.011$
6. Orbital Inclination, i_b (deg)	89.59	89.70	-0.16	$+0.50$
7. Relative Nodal Longitude, $\Delta\Omega_b$ (deg)	0.10	0.23	-0.21	$+0.58$
Planet c Orbit (Epoch BJD - 2,455,246.6545)				
8. Orbital Period, P_c (day)	303.158	303.137	-0.020	$+0.072$
9. Eccentricity Parameter, $\sqrt{e_c}\cos(\omega_c)$	-0.35	-0.04	-0.40	$+0.41$
10. Eccentricity Parameter, $\sqrt{e_c}\sin(\omega_c)$	-0.237	-0.257	-0.041	$+0.039$
11. Time of Barycentric Transit, t_c (BJD - 2,455,000)	246.985	246.997	-0.012	$+0.016$
12. Orbital Inclination, i_c (deg)	89.826	89.825	-0.010	$+0.009$
13. Relative Nodal Longitude, $\Delta\Omega_c$ (deg)	1.06	0.99	-0.50	$+0.49$
Stellar Orbit				
14. Orbital Period, P_{AB} (day)	7.44837695	7.44837703	-0.00000021	$+0.00000021$
15. Eccentricity Parameter, $e_{EB}\cos(\omega_{EB})$	-0.019778	-0.019797	-0.000045	$+0.000044$
16. Eccentricity Parameter, $e_{EB}\sin(\omega_{EB})$	-0.0125	-0.0112	-0.0019	$+0.0019$
17. Time of Primary Eclipse, t_{EB} (BJD - 2455000)	-29.306346	-29.306342	-0.000018	$+0.000018$
18. Orbital Inclination, i_{EB} (deg)	89.34	89.40	-0.10	$+0.12$
Radius/Light Parameters				
19. Linear Limb Darkening Parameter for Star A, u	0.4151	0.4137	-0.0044	$+0.0044$
20. Stellar Flux Ratio, F_B/F_A ($\times 100$)	0.568	0.579	-0.017	$+0.017$
21. Density of Star A, ρ_A (g cm^{-3})	1.163	1.176	-0.025	$+0.024$
22. Radius Ratio, Star B, R_B/R_A	0.3636	0.3671	-0.0047	$+0.0047$
23. Planetary Radius Ratio, R_b/R_A	0.0283	0.0289	-0.0011	$+0.0011$
24. Planetary Radius Ratio, R_c/R_A	0.0439	0.0440	-0.0018	$+0.0017$
Relative Contamination, $100 \times (F_{\rm cont}/F_A)$				
Season 0	-2.9	-0.9	-2.8	$+2.8$
Season 1	-1.5	0.5	-2.8	$+2.9$
Season 2	-2.8	-0.8	-2.8	$+2.8$
Season 3	-1.9	0.1	-2.8	$+2.9$
Noise Parameter				
Long Cadence Relative Width, $\sigma_{\rm LC}$ ($\times 10^5$)	62.95	62.75	-0.42	$+0.43$
Radial Velocity Parameters				
RV Offset, γ (km s^{-1})	4.67	4.60	-0.23	$+0.22$
Zero-level Diff., $\Delta\gamma$ (km s^{-1})	-0.12	-0.01	-0.31	$+0.30$
RV Jitter, σ_{RV} (km s^{-1})	0.31	0.43	-0.12	$+0.19$

Table S6: **Derived parameters from the photometric-dynamical model.**

Parameter	Best-fit	50%	15.8%	84.2%
Bulk Properties				
Mass of Star A, M_A ($M_\odot$)	1.043	1.049	-0.055	$+0.054$
Mass of Star B, M_B ($M_\odot$)	0.362	0.363	-0.013	$+0.012$
Radius of Star A, R_A ($R_\odot$)	0.964	0.963	-0.017	$+0.017$
Radius of Star B, R_B ($R_\odot$)	0.3506	0.3533	-0.0063	$+0.0060$
Radius of Planet b, R_b ($R_\oplus$)	2.98	3.03	-0.12	$+0.12$
Radius of Planet c, R_c ($R_\oplus$)	4.61	4.62	-0.20	$+0.20$
Density of Star A, ρ_A (g cm^{-3})	1.163	1.176	-0.025	$+0.024$
Density of Star B, ρ_B (g cm^{-3})	8.41	8.24	-0.20	$+0.21$
Gravity of Star A, $\log g_A$ (cgs)	4.488	4.492	-0.011	$+0.010$
Gravity of Star B, $\log g_B$ (cgs)	4.9073	4.9017	-0.0067	$+0.0067$
Orbital Properties				
Semimajor Axis of Stellar Orbit, a_{AB} (AU)	0.0836	0.0838	-0.0014	$+0.0013$
Semimajor Axis of Planet b, a_b (AU)	0.2956	0.2962	-0.0047	$+0.0044$
Semimajor Axis of Planet c, a_c (AU)	0.989	0.991	-0.016	$+0.015$
Eccentricity of Stellar Orbit, e_{AB}	0.0234	0.0228	-0.0009	$+0.0010$
Argument of Periapse Stellar Orbit, ω_{AB} (Degrees)	212.3	209.5	-4.4	$+4.1$
Mutual Orbital Inclination, I_b (deg)	0.27	0.43	-0.24	$+0.66$
Mutual Orbital Inclination, I_c (deg)	1.16	1.08	-0.42	$+0.46$
Eccentricities Constraints				
Eccentricity of Planet b Orbit (95% conf.), e_b	< 0.035			
Eccentricity of Planet c Orbit (95% conf.), e_c	< 0.411			

Table S7: **Predicted transit times for planet b.**

Epoch	T_0-2,455,000 BJD	Impact Parameter	Transit Velocity (R_A/day)	Duration (hr)
22	1025.630 ± 0.035	0.527 ± 0.237	6.007 ± 0.094	7.069 ± 0.963
23	1073.156 ± 0.022	0.602 ± 0.265	12.496 ± 0.136	3.209 ± 0.605
24	1121.106 ± 0.075	0.528 ± 0.236	4.522 ± 0.086	9.353 ± 1.339
25	1169.457 ± 0.033	0.642 ± 0.261	12.282 ± 0.111	3.170 ± 0.681
26	1216.768 ± 0.072	0.577 ± 0.246	7.221 ± 0.260	5.674 ± 0.960
27	1265.733 ± 0.050	0.691 ± 0.261	11.318 ± 0.129	3.280 ± 0.809
28	1312.836 ± 0.073	0.654 ± 0.255	9.880 ± 0.268	3.885 ± 0.847
29	1361.940 ± 0.081	0.742 ± 0.266	9.580 ± 0.264	3.667 ± 1.041
30	1409.062 ± 0.083	0.745 ± 0.269	11.584 ± 0.213	3.016 ± 0.852
31	1457.985 ± 0.149	0.774 ± 0.275	7.030 ± 0.490	4.897 ± 1.514
32	1505.349 ± 0.099	0.838 ± 0.288	12.403 ± 0.124	2.596 ± 0.840
33	1553.638 ± 0.299	0.783 ± 0.285	4.552 ± 0.261	7.406 ± 2.197
34	1601.654 ± 0.123	0.917 ± 0.312	12.433 ± 0.137	2.454 ± 0.872
35	1649.136 ± 0.281	0.835 ± 0.301	6.085 ± 0.750	5.389 ± 1.845
36	1697.947 ± 0.159	0.963 ± 0.342	11.752 ± 0.363	2.532 ± 0.949
37	1745.100 ± 0.235	0.917 ± 0.331	9.008 ± 0.752	3.496 ± 1.235
38	1794.188 ± 0.221	0.994 ± 0.374	10.313 ± 0.726	2.827 ± 1.076
39	1841.284 ± 0.229	0.993 ± 0.368	11.053 ± 0.532	2.678 ± 1.018
40	1890.314 ± 0.359	1.000 ± 0.403	8.063 ± 1.181	3.692 ± 1.560
41	1937.556 ± 0.243	1.053 ± 0.409	12.181 ± 0.256	2.402 ± 0.904
42	1986.153 ± 0.619	0.989 ± 0.425	5.333 ± 0.940	5.488 ± 2.230
43	2033.860 ± 0.275	1.090 ± 0.447	12.458 ± 0.233	2.257 ± 0.897
44	2081.589 ± 0.657	1.009 ± 0.445	5.096 ± 1.232	5.669 ± 2.273
45	2130.158 ± 0.328	1.106 ± 0.478	12.073 ± 0.675	2.389 ± 0.956
46	2177.380 ± 0.519	1.058 ± 0.472	7.999 ± 1.540	3.815 ± 1.701
47	2226.418 ± 0.429	1.093 ± 0.498	10.920 ± 1.298	2.676 ± 1.117
48	2273.503 ± 0.452	1.095 ± 0.498	10.406 ± 1.157	2.930 ± 1.211
49	2322.594 ± 0.652	1.059 ± 0.509	8.952 ± 1.842	3.420 ± 1.708
50	2369.745 ± 0.442	1.110 ± 0.516	11.826 ± 0.654	2.554 ± 1.039
51	2418.551 ± 0.948	1.027 ± 0.513	6.479 ± 1.596	4.824 ± 2.190
52	2466.039 ± 0.467	1.100 ± 0.522	12.314 ± 0.439	2.437 ± 0.942
53	2514.061 ± 1.048	1.007 ± 0.515	5.318 ± 1.565	5.741 ± 2.277
54	2562.341 ± 0.533	1.066 ± 0.516	12.245 ± 1.000	2.523 ± 0.980
55	2609.673 ± 0.888	1.007 ± 0.514	7.041 ± 2.193	4.574 ± 2.176
56	2658.612 ± 0.680	1.006 ± 0.499	11.336 ± 1.781	2.798 ± 1.204
57	2705.720 ± 0.731	1.003 ± 0.504	9.729 ± 1.868	3.343 ± 1.556
58	2754.815 ± 0.941	0.933 ± 0.477	9.607 ± 2.221	3.583 ± 1.858
59	2801.933 ± 0.665	0.977 ± 0.482	11.443 ± 1.205	2.886 ± 1.109

Table S7: (continued)

60	2850.864 ± 1.217	0.872 ± 0.453	7.453 ± 2.025	4.872 ± 2.182
61	2898.207 ± 0.665	0.931 ± 0.450	12.091 ± 0.809	2.810 ± 0.897
62	2946.504 ± 1.336	0.826 ± 0.428	6.071 ± 1.878	5.869 ± 2.223
63	2994.499 ± 0.731	0.874 ± 0.411	12.231 ± 1.283	2.896 ± 0.922
64	3041.964 ± 1.214	0.796 ± 0.400	6.417 ± 2.481	5.578 ± 2.385
65	3090.777 ± 0.898	0.799 ± 0.370	11.615 ± 1.982	3.255 ± 1.367
66	3137.912 ± 0.997	0.778 ± 0.366	9.062 ± 2.402	4.034 ± 1.866
67	3187.001 ± 1.142	0.713 ± 0.332	10.124 ± 2.354	3.862 ± 1.931
68	3234.085 ± 0.863	0.728 ± 0.329	11.034 ± 1.705	3.445 ± 1.234
69	3283.097 ± 1.385	0.623 ± 0.298	8.157 ± 2.238	4.894 ± 2.199
70	3330.344 ± 0.823	0.663 ± 0.292	11.893 ± 1.143	3.340 ± 0.832
71	3378.853 ± 1.505	0.548 ± 0.267	6.752 ± 2.073	6.129 ± 2.179
72	3426.633 ± 0.871	0.579 ± 0.265	12.139 ± 1.403	3.476 ± 1.016

Table S8: **Predicted transit times for planet c.**

Epoch	T_0-2,455,000 BJD	Impact Parameter	Transit Velocity (R_A/day)	Duration (hr)
3	1154.756 ± 0.011	0.430 ± 0.056	8.131 ± 0.133	4.735 ± 0.260
4	1458.197 ± 0.264	0.397 ± 1.258	3.369 ± 0.217	12.967 ± 1.000
5	1758.963 ± 0.024	0.446 ± 0.057	7.600 ± 0.135	5.086 ± 0.278
6	2062.831 ± 0.033	0.407 ± 0.114	7.249 ± 0.145	5.953 ± 0.462
7	2363.464 ± 0.076	0.458 ± 0.066	4.141 ± 0.258	9.823 ± 0.783
8	2667.055 ± 0.045	0.436 ± 0.116	8.195 ± 0.150	5.217 ± 0.417
9	2970.751 ± 0.085	0.462 ± 0.164	5.117 ± 0.316	9.026 ± 0.981
10	3271.295 ± 0.083	0.462 ± 0.118	6.923 ± 0.195	6.232 ± 0.487
11	3575.153 ± 0.080	0.461 ± 0.172	7.787 ± 0.236	5.922 ± 0.561

Table S9: **ELC model parameters.**

Parameter	Best fit
e	0.0306 ± 0.0071
ω (deg)	226 ± 12
R_A/a	0.05322 ± 0.00068
R_B/a	0.01935 ± 0.00029
$T_{\rm eff,B}/T_{\rm eff,A}$	0.5958 ± 0.0035
i (deg)	89.69 ± 0.16
x_A	0.30 ± 0.13
y_A	0.38 ± 0.27